Langtaosha (LTS) Preprint doi: https://doi.org/10.65215/LTSpreprints.2026.11.02.000378. This version posted November 2, 2026. The copyright holder for this preprint (which was not certified by peer review) is the author/funder. All Rights Reserved. No reuse allowed without permission.

Structural basis for the trafficking and function mechanism of the vesicular inhibitory amino acid transporter VIAAT

Pei Huang[1,2], Xiaoshuang Huang[1], Kaitong Guo[1], Feifan Yu[1,2], Xianglong Shen[1,2], Fangzhou Lu[1,2], Yuzhen Xie[1,2], Boyu Xie[3], Wayne Davis[4], Xiao Fan[1], Erik M. Jorgensen[4], and Jian Huang[1,5]

[1]Institute of Bio-Architecture and Bio-Interactions (IBABI), Shenzhen Medical Academy of Research and Translation (SMART), Shenzhen 518107, Guangdong, China.

[2]Westlake University, Hangzhou 310024, Zhejiang, China.

[3]Beijing Frontier Research Center for Biological Structures, State Key Laboratory of Membrane Biology, Tsinghua-Peking Joint Center for Life Sciences, School of Life Sciences, Tsinghua University, Beijing 100084, China.

[4]Howard Hughes Medical Institute (HHMI), School of Biological Sciences, University of Utah, Salt Lake City, UT 84112, USA.

[5]To whom correspondence should be addressed: Jian Huang (huangjian@smart.org.cn).

Langtaosha (LTS) Preprint doi: https://doi.org/10.65215/LTSpreprints.2026.11.02.000378. This version posted November 2, 2026. The copyright holder for this preprint (which was not certified by peer review) is the author/funder. All Rights Reserved. No reuse allowed without permission.

Abstract

The vesicular inhibitory amino acid transporter VIAAT packages γ-aminobutyric acid (GABA) and glycine into synaptic vesicles for fast inhibitory neurotransmission, yet its architecture, substrate recognition and association with trafficking-associated proteins remain poorly understood. Here we report cryo-EM structures of human VIAAT and its *Caenorhabditis elegans* orthologue UNC-47 at resolutions of 2.4-3.4 Å, each alone and in complex with their respective partners, LAMP5 and UNC-46, respectively. Both transporters adopt an eleven-transmembrane-helix architecture with a LeuT-like fold, but their partners engage them differently. LAMP5 binds hVIAAT primarily through its transmembrane helix, whereas the luminal domain of UNC-46 forms extensive contacts with UNC-47. A GABA-bound hVIAAT–LAMP5 structure delineates the substrate-binding pocket and local rearrangements accompanying occlusion, supported by mutational thermal-shift measurements. Comparison with a predicted cytosol-open model suggests an alternating access mechanism, while structure-based pKa calculations implicate Glu213 as the putative proton-coupling residue. Together, these findings establish a structural framework for inhibitory neurotransmitter transport and reveal evolutionary divergence in VIAAT-associated trafficking assemblies.

Langtaosha (LTS) Preprint doi: https://doi.org/10.65215/LTSpreprints.2026.11.02.000378. This version posted November 2, 2026. The copyright holder for this preprint (which was not certified by peer review) is the author/funder. All Rights Reserved. No reuse allowed without permission.

Introduction

The balance between excitatory and inhibitory neurotransmission is essential for neural circuit function. Disruption of this balance is associated with social deficits and a range of neurodevelopmental and psychiatric disorders[1-7]. Vesicular accumulation of inhibitory neurotransmitters supports quantal release during exocytosis[8]. Early genetic and functional studies identified the vesicular inhibitory amino acid transporter VIAAT (also known as VGAT), encoded by *SLC32A1*, as the transporter responsible for vesicular uptake of the inhibitory neurotransmitters GABA and glycine[9,10]. By packaging both transmitters, VIAAT supports GABAergic and glycinergic transmission and enables their co-release from terminals containing both neurotransmitters[8,11-13]. Inherited missense variants in *SLC32A1* have been associated with genetic epilepsy with febrile seizures plus (GEFS+), whereas *de novo* variants have been linked to developmental and epileptic encephalopathy (DEE)[14,15]. Functional analyses showed that these variants compromise inhibitory transmission by impairing vesicular filling or altering short-term synaptic plasticity[15].

In mammals, VIAAT is the sole member of the SLC32 family[16] and is structurally distinct from the SLC18 vesicular monoamine/acetylcholine transporters (VMATs and VAChT) and the SLC17 vesicular glutamate transporters (VGLUTs), which contain twelve transmembrane helices and adopt the major facilitator superfamily (MFS) fold[17-26]. VIAAT was initially predicted to contain ten transmembrane segments[9]. However, subsequent topology studies placed both its amino and carboxy termini on opposite sides of the membrane, implying an odd number of transmembrane helices[27]. Despite these studies, the

Langtaosha (LTS) Preprint doi: https://doi.org/10.65215/LTSpreprints.2026.11.02.000378. This version posted November 2, 2026. The copyright holder for this preprint (which was not certified by peer review) is the author/funder. All Rights Reserved. No reuse allowed without permission.

membrane topology and three-dimensional (3D) architecture of VIAAT have therefore remained unresolved.

Vesicular neurotransmitter uptake is coupled by the proton electrochemical gradient generated by the vacuolar H^+-ATPase. The driving force comprises both a pH gradient (ΔpH) and a membrane potential (Δφ)[28,29]. VMAT- and VAChT-mediated uptake depends mainly on ΔpH[30,31], whereas VGLUT-mediated transport is driven predominantly by Δφ[32-36]. VIAAT uses both components[37-40], but the underlying ion-coupling mechanism remained unsettled. Studies using isolated vesicles proposed a GABA/H^+ exchange mechanism[40]. This interpretation is consistent with uptake-associated proton efflux observed in single vesicles and neurons[41,42], as well as the more rapid initial efflux from GABAergic vesicles in intact synapses[43]. By contrast, reconstituted VIAAT was reported to mediate strictly Cl^--dependent, Δφ-driven transport, leading to a model in which GABA is co-transported with two chloride ions[44]. These findings have led to different models of VIAAT-mediated transport, leaving the molecular basis of ion coupling unresolved.

VIAAT function also depends on its correct targeting to synaptic vesicles[45-47]. This process involves intrinsic sorting signals, adaptor proteins and auxiliary factors. In *Caenorhabditis elegans*, UNC-46 promotes the synaptic-vesicle localization of UNC-47, the VIAAT orthologue. Loss of UNC-46 redistributes UNC-47 along axons and reduces the frequency of miniature inhibitory currents, with little effect on synaptic-vesicle abundance or the amplitude of the remaining currents. Moreover, overexpression of UNC-47 alleviates the

Langtaosha (LTS) Preprint doi: https://doi.org/10.65215/LTSpreprints.2026.11.02.000378. This version posted November 2, 2026. The copyright holder for this preprint (which was not certified by peer review) is the author/funder. All Rights Reserved. No reuse allowed without permission.

locomotor and enteric muscle contraction defects[48], supporting a primary role for UNC-46 in transporter trafficking rather than substrate transport. The mammalian orthologue LAMP5 exhibits selective neuronal expression, localizes to endocytic compartments and co-localizes with VIAAT at subsets of inhibitory terminals[49-51]. However, *Lamp5* deletion in mice alters short-term synaptic plasticity, startle responses and auditory processing without producing detectable VIAAT mislocalization[50,51]. Rat VGAT also contains an atypical amino-terminal dileucine-like motif involved in AP-2-dependent endocytosis[52]. These observations suggest that VIAAT trafficking relies on both intrinsic sorting signals and species-dependent accessory mechanisms.

Although human VIAAT and *C. elegans* UNC-47 occupy widely separated branches of the metazoan phylogeny and exhibit low sequence identity, they retain the same core function in vesicular GABA transport (Fig. 1a; Supplementary Fig. S1 and Tables S1-S2). Their trafficking-associated proteins, LAMP5 and UNC-46, appear less functionally equivalent. This contrast provides an opportunity to distinguish conserved features of the transport machinery from lineage-specific adaptations in transporter regulation and vesicular targeting. Whether LAMP5 and UNC-46 bind directly to their respective transporters, and how their modes of association relate to their different biological roles, remain unsolved. More broadly, the absence of structural information has limited understanding of VIAAT architecture, substrate recognition, alternating access and ion coupling.

Here we present cryo-EM structures of the human VIAAT–LAMP5 and *C. elegans*

Langtaosha (LTS) Preprint doi: https://doi.org/10.65215/LTSpreprints.2026.11.02.000378. This version posted November 2, 2026. The copyright holder for this preprint (which was not certified by peer review) is the author/funder. All Rights Reserved. No reuse allowed without permission.

UNC-47–UNC-46 complexes and examine their interfaces biochemically. Comparative structural and evolutionary analyses reveal a conserved VIAAT transport core accompanied by lineage-specific cytosolic features and divergent modes of accessory-protein engagement. A GABA-bound VIAAT–LAMP5 structure identifies the substrate-recognition features and associated local rearrangements. Together with a predicted cytosol-open conformation and structure-based pK_a calculations, these findings provide a framework for an alternating-access model of GABA transport and its coupling to the vesicular proton gradient.

Results

Structural determination of VIAAT complexes from evolutionarily distant species

To examine the structural organization of VIAAT in evolutionarily distant species, we selected human VIAAT (hVIAAT; UniProt Q9H598) and its *C. elegans* orthologue UNC-47 (UniProt P34579), which occupy widely separated branches of the metazoan phylogeny (Fig. 1a; Supplementary Fig. S1 and Tables S1-S2). Codon-optimized constructs encoding hVIAAT and UNC-47 were used for expression in HEK293F cells, either alone or co-expressed with their respective trafficking-associated partners, LAMP5 (UniProt Q9UJQ1) and UNC-46 (UniProt Q9GZD5; Supplementary Fig. S2 and Table S3). Using one-step affinity purification through the N-terminal FLAG tag on VIAAT, followed by size-exclusion chromatography, hVIAAT yielded a single, homogeneous peak whether expressed alone or co-expressed with LAMP5. By contrast, UNC-47 produced well-behaved protein samples only when co-expressed with UNC-46 (Supplementary Fig. S3a). Although LAMP5 is the closest human LAMP-family homologue of UNC-46 (Supplementary Fig. S2), the two

Langtaosha (LTS) Preprint doi: https://doi.org/10.65215/LTSpreprints.2026.11.02.000378. This version posted November 2, 2026. The copyright holder for this preprint (which was not certified by peer review) is the author/funder. All Rights Reserved. No reuse allowed without permission.

VIAAT orthologues showed different biochemical dependence on their respective partners during purification.

Following well-established protocols for cryo-sample preparation, data acquisition, and processing, we obtained three-dimensional (3D) reconstructions of the apo hVIAAT–LAMP5 and UNC-47–UNC-46 complexes at overall resolutions of 3.0 Å and 2.4 Å, respectively (Fig. 1b,c; Supplementary Figs. S4-S7 and Table S4). Additional reconstructions of apo hVIAAT alone at 3.4 Å and partner-free UNC-47 at 2.8 Å are described in the Supplementary Information (Supplementary Figs. S3b,c and S7 and Table S4). The partner-free UNC-47 population was identified by deeper 3D-classification of the UNC-47–UNC-46 co-expression dataset (Supplementary Fig. S4). In the UNC-47–UNC-46 complex reconstruction, the transmembrane regions and the UNC-46 luminal domain were resolved at sufficient resolution for atomic modelling (Fig. 1c; Supplementary Figs. S6 and S7). In the hVIAAT–LAMP5 complex reconstruction, the transmembrane region was resolved at high resolution, whereas the lower local resolution of the LAMP5 luminal domain supported placement of an overall model but not detailed side-chain assignment (Fig. 1b; Supplementary Figs. S5 and S7).

LAMP5 contained a single transmembrane helix connected to a luminal domain. UNC-46 was anchored in a similar manner, but its luminal domain adopted a markedly different orientation and formed extensive contacts with the luminal surface of UNC-47. Densities consistent with N-linked glycans were observed at Asn35, Asn146 and Asn166 of

Langtaosha (LTS) Preprint doi: https://doi.org/10.65215/LTSpreprints.2026.11.02.000378. This version posted November 2, 2026. The copyright holder for this preprint (which was not certified by peer review) is the author/funder. All Rights Reserved. No reuse allowed without permission.

UNC-46 (Fig. 1c). Several lipid-like densities were resolved at the protein-membrane interfaces of both complexes. Additional densities associated with Cys421 of hVIAAT and the evolutionarily corresponding Cys383 of UNC-47 were consistent with palmitoylation of these residues (Fig. 1b,c). Together, these structures show that human and *C. elegans* VIAAT associate with single-pass LAMP-family partners, while revealing pronounced divergence in the arrangement of their luminal domains.

Conserved VIAAT transport cores contain lineage-specific cytosolic elements

Both hVIAAT and UNC-47 adopted an 11-transmembrane-helix architecture comprising a pseudosymmetric transport core and a peripheral TM11 (Fig. 2a,b). The core contained two inverted structural repeats formed by TM1-TM5 and TM6-TM10. TM1 and TM6 were interrupted near the centre of the membrane, generating the characteristic unwound segments that face the central substrate-binding region. These features are characteristic of the LeuT-like protein fold (Supplementary Fig. S8). Cross-sectional views of the electrostatic surfaces revealed a central cavity in each transporter, which opened towards the vesicle lumen but remained sealed on the cytosolic side, placing both transporters in luminal-open conformations (Fig. 2c). Despite their sequence divergence, the transport cores of hVIAAT and UNC-47 superimposed closely across most transmembrane helices, indicating that the overall architecture required for inhibitory amino acid transport is conserved.

The principal structural difference occurred on the cytosolic side. In hVIAAT, the extended loop between TM2 and helix H1 encompassed residues 171-184 and formed two

Langtaosha (LTS) Preprint doi: https://doi.org/10.65215/LTSpreprints.2026.11.02.000378. This version posted November 2, 2026. The copyright holder for this preprint (which was not certified by peer review) is the author/funder. All Rights Reserved. No reuse allowed without permission.

short antiparallel β-strands, β1 and β2 (Fig. 2d). This loop contained six acidic residues, Glu172, Glu173, Glu175, Asp176, Glu178 and Asp184, together with two basic residues Arg181 and Arg183, giving the region a pronounced net-negative charge. The corresponding segment in UNC-47 was shorter and had a markedly different charge distribution.

Comparison of this region across representative metazoans placed the structural difference in a broader evolutionary context (Extended Data Fig. S9a). Longer loops were present in the sampled cnidarian, several non-nematode protostomes and non-vertebrate deuterostomes. By contrast, the shorter form was concentrated in nematodes and was approximately five residues shorter than the loops of most other species examined. Glutamate and aspartate residues were already enriched in the hemichordate and cephalochordate sequences, although their negative charge was partly offset by lysine and arginine residues. Among the species sampled, a pronounced net-negative charge was first evident in the lamprey *Petromyzon marinus* and was retained in cartilaginous fishes, bony fishes and tetrapods. This distribution is consistent with a stably net-negative loop emerging near the base of the vertebrate lineage.

Given its position near the cytosolic vestibule, variation in loop length and the enrichment of acidic residues could alter local flexibility and surface electrostatics. The loop may therefore provide a lineage-dependent site for regulation or trafficking, but its functional role remains to be tested.

Langtaosha (LTS) Preprint doi: https://doi.org/10.65215/LTSpreprints.2026.11.02.000378. This version posted November 2, 2026. The copyright holder for this preprint (which was not certified by peer review) is the author/funder. All Rights Reserved. No reuse allowed without permission.

LAMP5 and UNC-46 engage VIAAT through distinct assembly modes

Superposition of the hVIAAT–LAMP5 and UNC-47–UNC-46 complexes revealed that LAMP5 and UNC-46 bind to the same general face of the VIAAT transport core but adopt substantially different orientations (Fig. 3a). In both complexes, the single transmembrane helix of LAMP5 or UNC-46 was positioned adjacent to TM4 and TM9 of VIAAT. However, the relative orientations of their membrane-proximal and luminal domains differed, resulting in distinct overall assemblies.

At the hVIAAT–LAMP5 interface, the LAMP5 transmembrane helix packed against TM4 and TM9 of hVIAAT through extensive hydrophobic contacts. Within this region, the side chain of LAMP5 Tyr256 formed a hydrogen bond with the backbone carbonyl oxygen of hVIAAT Leu428 in TM9 (Fig. 3b, *left*). Additional contacts occurred on the luminal side, where the membrane-proximal region of LAMP5 approached the luminal end of TM4 and loop L3-4, which connects TM3 and TM4. LAMP5 Arg230 formed hydrogen bonds with the backbone carbonyls of hVIAAT Pro234, Gly235 and Leu236, whereas the backbone carbonyl of LAMP5 Glu234 contacted hVIAAT Ser239 in TM4 (Fig. 3c, *left*).

UNC-46 engaged the corresponding TM4-TM9 surface of UNC-47 predominantly through hydrophobic contacts, but its transmembrane interface contained a more extensive network of polar interactions (Fig. 3b, *right*). In the central portion of the membrane, UNC-46 Ser227 contacted the backbone carbonyl of UNC-47 Ala210, and UNC-46 His231 contacted UNC-47 Thr214. Near the cytosolic end, UNC-46 His235 formed a hydrogen bond

Langtaosha (LTS) Preprint doi: https://doi.org/10.65215/LTSpreprints.2026.11.02.000378. This version posted November 2, 2026. The copyright holder for this preprint (which was not certified by peer review) is the author/funder. All Rights Reserved. No reuse allowed without permission.

with the backbone carbonyl of UNC-47 Leu390, whereas Arg239 contacted UNC-47 Ser385, Ser389 and Glu392. The luminal side of the UNC-47–UNC-46 interface was more elaborate. UNC-46 bent towards the transporter, positioning helices H1' and H2' against the membrane-proximal surface of UNC-47 (Fig. 3c, *right*). The backbone carbonyl of UNC-46 Ser203 contacted UNC-47 Gln193 in TM3, while UNC-46 Arg206 formed a hydrogen bond with UNC-47 Asp200 in TM4. A water-mediated network further connected UNC-46 Arg206 and Ser211 to UNC-47 Lys201. Beyond these membrane-proximal contacts, the UNC-46 luminal domain formed an extended interaction network with the luminal surface of UNC-47 (Fig. 3d). No equivalent luminal interface was observed in the hVIAAT–LAMP5 complex.

We next examined these interaction modes using reciprocal pull-down assays. The VIAAT transport core carried a FLAG tag, whereas each LAMP-family partner carried a Twin-Strep tag, allowing either component to serve as the affinity handle. Wild-type hVIAAT and LAMP5 were recovered together in both pull-down directions, as were wild-type UNC-47 and UNC-46, confirming stable association within each pair (Fig. 3e). To test the polar contacts at the hVIAAT–LAMP5 interface, we introduced the R230A and Y256A substitutions into LAMP5. The double substitution weakened the formation of the complex. Combining these substitutions with S239A in hVIAAT produced a more pronounced loss of association (Fig. 3e, *left*). Consistently, size-exclusion chromatography of the anti-FLAG eluates revealed a later elution peak for the hVIAAT(S239A)–LAMP5(R230A/Y256A) co-expression sample compared to the wild-type complex, indicating a smaller particle size and further supporting impaired complex formation (Extended Data Fig. S10a). Together, these

Langtaosha (LTS) Preprint doi: https://doi.org/10.65215/LTSpreprints.2026.11.02.000378. This version posted November 2, 2026. The copyright holder for this preprint (which was not certified by peer review) is the author/funder. All Rights Reserved. No reuse allowed without permission.

results indicate that the polar-contact network observed in the structure contributes to the stability of the hVIAAT–LAMP5 complex.

The extensive and distributed UNC-47–UNC-46 interface made it difficult to identify point mutations that would disrupt complex formation. We therefore designed two domain-swapped chimeras to dissect the contributions of the luminal and membrane-associated regions. Chimera 1 comprised the LAMP5 luminal domain fused to the transmembrane and membrane-proximal regions of UNC-46, including helices H1' and H2'. Chimera 2 contained the UNC-46 luminal domain fused to the LAMP5 transmembrane region. In reciprocal pull-down assays, chimera 1 showed markedly reduced association with hVIAAT, whereas Chimera 2 retained binding and was recovered at least as efficiently as wild-type LAMP5 (Fig. 3e, *middle*). These findings indicated that the interaction between hVIAAT and LAMP5 is primarily mediated by the transmembrane and membrane-proximal regions of LAMP5, with a comparatively limited contribution from its luminal domain. By contrast, both chimeras showed reduced association with UNC-47 (Fig. 3e, *right*). Consistent with the pull-down results, co-expression with either chimera reduced the chromatographic homogeneity of UNC-47, yielding SEC profiles resembling that of UNC-47 expressed alone (Extended Data Figs. S3a and S10b). Retaining either the UNC-46 luminal domain or its transmembrane region alone was therefore insufficient to preserve wild-type complex formation. These results are consistent with the structural observations, supporting that both the luminal and membrane-associated regions of UNC-46 contribute to stable association with UNC-47.

Langtaosha (LTS) Preprint doi: https://doi.org/10.65215/LTSpreprints.2026.11.02.000378. This version posted November 2, 2026. The copyright holder for this preprint (which was not certified by peer review) is the author/funder. All Rights Reserved. No reuse allowed without permission.

To determine whether these assembly differences extended across metazoan evolution, we mapped the predicted luminal-domain-transporter interface area onto a phylogeny of representative LAMP-family proteins (Fig. 3f; Supplementary Fig. S11 and Tables S5-S7). The calculated interface varied substantially among species. Large luminal interfaces were common among nematode UNC-46 homologues, including that of *C. elegans*, and also occurred in several other invertebrate lineages. Vertebrate LAMP5 homologues generally displayed smaller interfaces. Accordingly, the experimentally determined UNC-47–UNC-46 and hVIAAT–LAMP5 complexes lay towards opposite ends of the predicted distribution. Representative AlphaFold 3 models showed a corresponding difference in complex geometry. Proteins with large calculated interface areas positioned their luminal domains against the VIAAT transport core, whereas proteins with smaller interfaces contacted VIAAT mainly through their transmembrane and membrane-proximal regions (Fig. 3f; Supplementary Table S7). Considerable variation remained among non-vertebrate species, and some vertebrates retained intermediate interface areas, arguing against a uniform stepwise transition. Nevertheless, the overall distribution is consistent with extensive luminal engagement being retained in several invertebrate lineages, particularly nematodes, and reduced in the vertebrate LAMP5 lineage.

Structural basis of GABA recognition by human VIAAT

To define how VIAAT recognizes its principal neurotransmitter substrate GABA, we determined the cryo-EM structure of the GABA-bound hVIAAT–LAMP5 complex at an overall resolution of 2.9 Å (Fig. 4a; Supplementary Figs. S5 and S7 and Table S4). A non-

Langtaosha (LTS) Preprint doi: https://doi.org/10.65215/LTSpreprints.2026.11.02.000378. This version posted November 2, 2026. The copyright holder for this preprint (which was not certified by peer review) is the author/funder. All Rights Reserved. No reuse allowed without permission.

protein density was observed within the central cavity of hVIAAT and could be modelled as GABA. The binding site was located approximately halfway across the membrane and was formed primarily by residues from TM1, TM3 and TM6 (Fig. 4b). The amino group of GABA formed hydrogen bonds with the Tyr221 side chain and the backbone carbonyl of Met132, while its carboxylate group contacted Thr318. A resolved water molecule further completed the local polar-interaction network, and Phe315 formed hydrophobic contacts with the carbon backbone of GABA. The pocket therefore recognizes GABA through a combination of direct polar coordination and shape complementarity.

Comparison of the GABA-bound and apo structures showed that GABA binding induced local rearrangements around the pocket rather than a large-scale movement of the transporter core (Fig. 4c). Met132, Tyr221, Phe315 and Thr318 shifted towards the bound substrate, reducing the volume of the binding pocket. Phe315 underwent the largest side-chain displacement, while smaller movements of Tyr221 and Thr318 completed the polar-contact network. These changes converted the more open apo pocket into a compact, substrate-bound luminal-occluded state.

We assessed the contributions of these residues to GABA recognition using a GABA-dependent thermal-shift assay (Fig. 4d; Supplementary Table S8). GABA produced a robust stabilization of wild-type hVIAAT, with an increased melting temperature by 4.46 ± 0.09 °C (ΔT_m; mean ± s.e.m.). Substitution of Y221 with alanine almost abolished this stabilization, whereas Y221F retained a partial response, with a ΔT_m of 1.43 ± 0.16 °C. F315A and T318A

Langtaosha (LTS) Preprint doi: https://doi.org/10.65215/LTSpreprints.2026.11.02.000378. This version posted November 2, 2026. The copyright holder for this preprint (which was not certified by peer review) is the author/funder. All Rights Reserved. No reuse allowed without permission.

variants showed intermediate ΔT_m values of 2.52 ± 0.13 ℃ and 2.44 ± 0.31 ℃, respectively. The effects of Y221A and Y221F indicate that both the hydroxyl group and aromatic ring of Y221 contribute to GABA recognition. The hydroxyl group provides direct polar coordination, whereas the aromatic side chain helps define the shape and chemical environment of the binding pocket. Sequence comparison of VIAAT orthologues from 27 representative metazoans further revealed the strong conservation of these binding residues (Supplementary Fig. S9b). Collectively, the structural, biochemical and evolutionary analyses identify Tyr221, Phe315 and Thr318 as key determinants of GABA recognition across VIAAT orthologues.

Conformational transitions underlying GABA transport

The apo and GABA-bound structures captured hVIAAT in two related lumen-facing conformations. To examine other states of the alternating-access cycle, we generated a putative cytosol-open model using AlphaFold 3 through the AlphaFold Server. Comparison of this model with the experimentally determined structures suggested a plausible sequence of conformational states, progressing from the cytosol-open state to the GABA-bound luminal-occluded state, and finally to the apo luminal-open state (Fig. 5a, *top*). In the putative cytosol-open model, a solvent-accessible pathway extended from the cytosol to the central substrate-binding pocket. This pathway was closed in the GABA-bound structure, in which the pocket formed a compact, occluded cavity. The apo structure instead displayed an expanded luminal vestibule, consistent with opening of the luminal gate after substrate release (Fig. 5a, *middle*).

Langtaosha (LTS) Preprint doi: https://doi.org/10.65215/LTSpreprints.2026.11.02.000378. This version posted November 2, 2026. The copyright holder for this preprint (which was not certified by peer review) is the author/funder. All Rights Reserved. No reuse allowed without permission.

To resolve the local changes associated with these transitions, we aligned the three structures using TM3, TM4, TM8 and TM9 as the scaffold domain and compared residues surrounding the substrate-binding pocket. Three phenylalanine residues, Phe133, Phe315 and Phe322, underwent state-dependent rearrangements that may contribute to gating (Fig. 5a, *bottom*). During the proposed transition from the cytosol-open to the luminal-occluded state, Phe322 moved towards the central pocket and the scaffold domain, narrowing the cytosolic pathway. The luminal pathway remained closed at this stage, although Phe133 and Phe315 shifted slightly away from the pocket. The subsequent transition to the apo luminal-open structure involved a larger outward displacement of Phe315, accompanied by a smaller movement of Phe133. These changes expanded the luminal side of the central cavity and provided a route for substrate release.

Alignment of the putative cytosol-open model and the apo luminal-open structure on their scaffold domains also revealed broader movements of the transport bundle (Fig. 5b). The largest displacements occurred in TM1 and TM6, with additional changes in TM2, TM7 and TM11. TM1a and TM6b, together with the cytosolic portions of TM2, TM7 and TM10, moved towards the scaffold domain. On the opposite side of the membrane, TM1b and TM6a and the luminal portions of TM2, TM7 and TM5 moved away from the scaffold. These opposing movements reversed the direction of solvent access to the central cavity. TM11 followed the overall motion of the bundle but did not contribute directly to the substrate-binding pocket. The luminal end of TM10 and the cytosolic end of TM5 moved comparatively little and therefore marked apparent pivot regions for the conformational

Langtaosha (LTS) Preprint doi: https://doi.org/10.65215/LTSpreprints.2026.11.02.000378. This version posted November 2, 2026. The copyright holder for this preprint (which was not certified by peer review) is the author/funder. All Rights Reserved. No reuse allowed without permission.

rearrangement (Fig. 5b).

Distinct polar-interaction networks accompanied closure of the luminal and cytosolic gates. In the putative cytosol-open model, the luminal vestibule was sealed by residues including Asn231, Glu368, Thr371, Asp372, Arg379 and Asn383 (Fig. 5c). Glu368 formed hydrogen bonds with the backbone amide groups of Phe453 and Ala454. Asp372 contacted Asn231, Arg379 and Asn383, while Asn383 also interacted with Thr371. This network is positioned to stabilize closure of the luminal pathway in the predicted cytosol-open state. In the luminal-open structure, a separate network sealed the cytosolic side of the transporter (Fig. 5d). Glu120, Asn124 and Asn127 in TM1 formed an interconnected hydrogen-bonding network with Lys261, Ser264, Ser267 and Ser393. Glu327 in TM6b additionally contacted Tyr171 and Arg181 within the cytosolic loop between TM2 and helix H1. Exchange between these luminal and cytosolic interaction networks could therefore contribute to the alternating closure of the two gates.

Glu213 lay near the central transport pathway and showed different solvent exposure across the three conformations (Fig. 5a; Supplementary Fig. S12a). Its location is compatible with a role in proton coupling, although proton transfer cannot be inferred directly from static structures. Previous biochemical measurements placed the pH of the synaptic-vesicle lumen at approximately pH 5.5[53,54], whereas the presynaptic cytosol is maintained near neutral, typically at pH 7.0-7.2[55]. Structure-based PROPKA calculations produced pK_a values of 7.08, 7.20 and 7.51 for Glu213 in the cytosol-open, luminal-occluded and luminal-open states,

Langtaosha (LTS) Preprint doi: https://doi.org/10.65215/LTSpreprints.2026.11.02.000378. This version posted November 2, 2026. The copyright holder for this preprint (which was not certified by peer review) is the author/funder. All Rights Reserved. No reuse allowed without permission.

respectively. The progressive shift indicates that the predicted proton affinity of Glu213 is sensitive to the surrounding conformational environment. At the approximate cytosolic pH of 7.2, Glu213 in the cytosol-open model was predicted to be 56.9% deprotonated (GLU^- form) and 43.1% protonated (GLH form). In the luminal-occluded state, the predicted populations at the same pH were equal. At the vesicle-lumen pH of 5.5, the protonated state (GLH form) was strongly favored, with Glu213 predicted to be 98.0% protonated in the luminal-occluded structure and 99.0% protonated in the luminal-open structure (Supplementary Fig. S12b). These calculations are consistent with proton uptake from the acidic vesicle lumen and proton release into the cytosol, opposite to the direction of GABA transport.

Based on the two experimental structures and the putative cytosol-open model, we propose an alternating-access model for VIAAT-mediated GABA transport (Fig. 5e). In the cytosol-open state, the predominantly deprotonated population of Glu213 at pH 7.2 is compatible with proton release into the cytosol before or during GABA binding. Coordination of GABA then promotes closure of the cytosolic pathway, producing a luminal-occluded intermediate. Rearrangement of the transport bundle subsequently opens the luminal vestibule and permits GABA release into the synaptic-vesicle lumen. Exposure to the acidic lumen favors protonation of Glu213, after which the proton-bound transporter can return towards the cytosol-facing state. Release of the proton into the cytosol would reset the transporter for another round of GABA uptake. This model places GABA and proton movement in opposite directions and assigns alternating access to conformational changes intrinsic to the VIAAT transport core.

Langtaosha (LTS) Preprint doi: https://doi.org/10.65215/LTSpreprints.2026.11.02.000378. This version posted November 2, 2026. The copyright holder for this preprint (which was not certified by peer review) is the author/funder. All Rights Reserved. No reuse allowed without permission.

Discussion

Our findings reveal how the conserved transport machinery of VIAAT has evolved distinct molecular interactions with trafficking-associated partners. Despite sharing a conserved transport architecture, human VIAAT and its *C. elegans* orthologue UNC-47 exhibit markedly distinct modes of association with LAMP5 and UNC-46, respectively. Whereas LAMP5 engages hVIAAT primarily through its transmembrane and membrane-proximal regions, UNC-46 forms a more extensive interface involving both its transmembrane and luminal domains. These structural differences provide a potential molecular explanation for previous observations that UNC-46 is required for proper UNC-47 localization in *C. elegans*, whereas LAMP5 modulates inhibitory synaptic function but is dispensable for VIAAT localization in mammals[48,50,51]. The evolutionary divergence of these interaction interfaces further suggests that LAMP-family proteins have acquired lineage-specific regulatory roles rather than retaining a universally conserved mechanism of VIAAT trafficking and regulation.

Evolutionary diversification may also extend to regulatory elements within VIAAT itself. The acidic cytosolic β-hairpin identified in hVIAAT differs from the shorter corresponding region in UNC-47 and is distinct from the N-terminal sorting signal previously implicated in VGAT endocytosis[52]. Given that acidic sequence motifs also contribute to the intracellular targeting of other vesicular neurotransmitter transporters[56,57], this vertebrate-associated structural element may provide an additional interaction surface for proteins involved in VIAAT trafficking or regulation. The presence of this element may have

Langtaosha (LTS) Preprint doi: https://doi.org/10.65215/LTSpreprints.2026.11.02.000378. This version posted November 2, 2026. The copyright holder for this preprint (which was not certified by peer review) is the author/funder. All Rights Reserved. No reuse allowed without permission.

accompanied the evolutionary remodeling of LAMP-family interactions, potentially introducing additional mechanisms for controlling VIAAT localization and trafficking in vertebrates.

Beyond these regulatory interactions, our structures provide mechanistic insights into substrate recognition and transport by VIAAT. The GABA-bound hVIAAT–LAMP5 structure reveals a defined substrate-binding pocket and local conformational rearrangements associated with substrate occlusion. Together with comparison to a predicted cytosol-open conformation, these observations support an alternating-access mechanism in which substrate recognition is coupled to coordinated conformational changes that regulate access to the central binding pocket. The location of Glu213 and its potentially conformation-dependent proton affinity suggest a role in coupling substrate translocation to the vesicular proton electrochemical gradient, consistent with previous evidence supporting GABA/H^+ exchange[40-43]. Although chloride-dependent transport has also been reported[44], the absence of a clearly resolved chloride-binding site raises the possibility that chloride binds transiently during the transport cycle or influences transport through an indirect regulatory mechanism. Further functional and structural studies will be needed to clarify the precise contributions of protonation and chloride to the transport mechanism.

Taken together, our findings establish a structural framework connecting the conserved mechanism of inhibitory neurotransmitter transport with the evolutionary diversification of VIAAT-associated regulatory machinery. By revealing how VIAAT

Langtaosha (LTS) Preprint doi: https://doi.org/10.65215/LTSpreprints.2026.11.02.000378. This version posted November 2, 2026. The copyright holder for this preprint (which was not certified by peer review) is the author/funder. All Rights Reserved. No reuse allowed without permission.

preserves its core transport architecture while adopting distinct trafficking-associated assemblies and potentially additional intrinsic regulatory elements, our study provides molecular insights into the coordination of synaptic vesicle filling, transporter trafficking and inhibitory neurotransmission.

Langtaosha (LTS) Preprint doi: https://doi.org/10.65215/LTSpreprints.2026.11.02.000378. This version posted November 2, 2026. The copyright holder for this preprint (which was not certified by peer review) is the author/funder. All Rights Reserved. No reuse allowed without permission.

Materials and Methods

Cell culture and transient protein expression

HEK293F suspension cells (gift from Sino Biological Inc.) were maintained in SMM 293T-II medium (Sino Biological Inc.) at 37 °C under 5% CO_2 and 60% humidity. Codon-optimized cDNAs encoding full-length *C. elegans* UNC-47 (UniProt P34579) and human VIAAT (UniProt Q9H598) lacking the disordered N-terminal region (residues 1-109) were cloned into pCAG expression vectors separately with an N-terminal FLAG tag. Codon-optimized cDNAs encoding full-length *C. elegans* UNC-46 (UniProt Q9GZD5) and human LAMP5 (UniProt Q9UJQ1) were cloned into pCAG vectors separately with an N-terminal Strep tag. The truncated human VIAAT is hereafter referred to as hVIAAT. All constructs were verified by DNA sequencing before transfection.

For transient expression, HEK293F cells were transfected at a density of 1.5-2.0 × 10^6 cells mL^{-1}. For co-expression of hVIAAT with LAMP5 or UNC-47 with UNC-46, the corresponding expression plasmids were co-transfected at a concentration of 1 mg L^{-1} culture per plasmid using 40-kDa linear polyethylenimine (PEI; Hieff Trans® PEI MW40000, YEASEN) at 4 mg L^{-1} culture. For expression of hVIAAT alone, cells were transfected with the hVIAAT expression plasmid at 1.5 mg L^{-1} culture, using the same PEI reagent at 3 mg L^{-1} culture. Cells were harvested 48 h after transfection for subsequent protein purification.

Protein purification of human VIAAT–LAMP5 and *C. elegans* UNC-46–UNC-47 complexes

Langtaosha (LTS) Preprint doi: https://doi.org/10.65215/LTSpreprints.2026.11.02.000378. This version posted November 2, 2026. The copyright holder for this preprint (which was not certified by peer review) is the author/funder. All Rights Reserved. No reuse allowed without permission.

Cell pellets from 1 L of transfected HEK293F culture were resuspended in lysis buffer containing 25 mM Tris-HCl pH 7.5 and 150 mM NaCl. Membrane proteins were extracted in buffer containing 25 mM Tris-HCl pH 7.5, 150 mM NaCl, aprotinin (MCE; 3.9 mg mL^{-1}), pepstatin A (MCE; 2.1 mg mL^{-1}), leupeptin (MCE; 15 mg mL^{-1}) and 1% (w/v) lauryl maltose neopentyl glycol (LMNG; Anatrace). The suspension was incubated for 2 h at 4 °C with gentle rotation and centrifuged at 16,000 × g for 1 h at 4 °C. The supernatant was then incubated with anti-FLAG affinity resin (Sigma-Aldrich) for 1 h at 4 °C with gentle rotation.

The resin was washed three times with wash buffer containing 25 mM Tris-HCl pH 7.5, 150 mM NaCl, aprotinin (1.3 mg mL^{-1}), pepstatin A (0.7 mg mL^{-1}), leupeptin (5 mg mL^{-1}) and 0.01% (w/v) LMNG. The bound proteins were eluted in wash buffer supplemented with 0.4 mg mL^{-1} FLAG peptide. The eluate was then concentrated using 50-kDa molecular-weight-cut-off Amicon filter units (Millipore) and subjected to size-exclusion chromatography (SEC) on a Superose 6 Increase 10/300 GL column (GE Healthcare). The column was pre-equilibrated with running buffer containing 25 mM Tris-HCl pH 7.5, 150 mM NaCl, aprotinin (1.3 mg ml^{-1}), pepstatin A (0.7 mg ml^{-1}), leupeptin (5 mg ml^{-1}) and 0.01% (w/v) LMNG. Peak fractions containing the target protein or protein complex were pooled and concentrated for downstream structural studies. Sample purity was assessed by SDS-PAGE.

For preparation of the GABA-bound hVIAAT–LAMP5 complex, GABA (MACKLIN) was added to the extraction buffer at a final concentration of 50 mM and maintained throughout

Langtaosha (LTS) Preprint doi: https://doi.org/10.65215/LTSpreprints.2026.11.02.000378. This version posted November 2, 2026. The copyright holder for this preprint (which was not certified by peer review) is the author/funder. All Rights Reserved. No reuse allowed without permission.

purification. The Tris-HCl concentration was increased to 50 mM in the purification buffers accordingly to minimize changes in pH associated with the high GABA concentration. During SEC, the LMNG concentration was reduced to 0.001% (w/v). Peak fractions containing the GABA-bound hVIAAT–LAMP5 complex were pooled and concentrated for cryo-EM studies.

Cryo-EM sample preparation and data acquisition

Ni-Ti grids (M01-Au300-R1.2/1.3, Nano Dimension Ltd.) were glow-discharged immediately before use. Freshly purified hVIAAT and UNC-47 in their apo forms or in complex with their respective chaperones, with or without GABA, were applied to the grids in a Vitrobot Mark IV chamber maintained at 8 °C and 100% humidity. After blotting for 3.5 s, the grids were plunge-frozen in liquid ethane and stored in liquid nitrogen.

Cryo-EM data were collected on a 300-kV Titan Krios G4 electron microscope (Thermo Fisher Scientific) equipped with a Gatan K3 direct electron detector and a GIF Quantum energy filter. Movies were acquired using a Falcon IVi detector (Thermo Fisher Scientific) in electron-counting (EC) mode at a nominal magnification of ×130,000, corresponding to a calibrated pixel size of 0.936 Å. The nominal defocus range was set to -1.2 to -1.6 µm. Movie stacks were recorded in EER format using EPU software (Thermo Fisher Scientific), with a preset beam-spot size of 0.79 µm and a total electron exposure of approximately 50 e^{-} $Å^{-2}$ per movie.

Langtaosha (LTS) Preprint doi: https://doi.org/10.65215/LTSpreprints.2026.11.02.000378. This version posted November 2, 2026. The copyright holder for this preprint (which was not certified by peer review) is the author/funder. All Rights Reserved. No reuse allowed without permission.

Cryo-EM data processing

UNC-47 dataset: A total of 2,470 cryo-EM micrographs were collected for the UNC-47–UNC-46 complex sample. Preprocessing steps, including motion correction and CTF estimation, were performed using cryoSPARC Live. An initial set of 1,912,160 particles was picked using a pretrained general Topaz model, extracted with 2x binning (bin-2), and subjected to 2D classification. Particles from 2D class averages displaying well-defined secondary structural features were selected for ab initio reconstruction into 5 classes (K=5). 516,343 particles from the two best-resolved ab initio classes were selected for an additional round of 2D classification cleaning. The resulting particles were then used to re-train a new Topaz model, which was subsequently applied to repick 2,976,695 particles from the micrographs. These particles were again extracted in bin-2 and subjected to heterogeneous refinement using two high-quality references from ab initio reconstructions and two decoy junk references. After the first round of heterogeneous refinement, particles assigned to the two junk classes underwent an additional round of 2D classification and selection. The selected particles were then combined with those assigned to good 3D classes. Subsequently, 2,246,589 particles were re-extracted without binning and subjected to multiple rounds of heterogeneous refinement. 285,342 particles were selected for another round of ab initio reconstruction (K=3), resolving a distinct class corresponding to UNC-47 alone. Direct non-uniform refinement of the 150,565 particles from the UNC-47 alone class yielded a 2.8 Å reconstruction (Supplementary Fig. S4).

The UNC-47–UNC-46 complex class obtained from ab initio reconstruction was used as a

Langtaosha (LTS) Preprint doi: https://doi.org/10.65215/LTSpreprints.2026.11.02.000378. This version posted November 2, 2026. The copyright holder for this preprint (which was not certified by peer review) is the author/funder. All Rights Reserved. No reuse allowed without permission.

reference in heterogeneous refinement to recover additional complex particles from those discarded during earlier processing. Non-uniform refinement of 421,169 selected particles yielded a 2.4 Å reconstruction of the UNC-47–UNC-46 complex (Supplementary Fig. S4).

hVIAAT dataset: A total of 3,094/2,470/4,705 cryo-EM micrographs were collected for the hVIAAT alone, hVIAAT–LAMP5 complex and hVIAAT–LAMP5 with GABA datasets, respectively. Preprocessing and reconstruction were performed using cryoSPARC, following the procedures described above for the UNC-47 dataset. A total of 2,366,997/2,199,315/2,139,359 particles were initially picked using the same pretrained Topaz model. The particles were subsequently extracted and subjected to iterative rounds of 2D classification and heterogeneous refinement, yielding 1,374,848/1,164,868/1,226,188 particles assigned to well-resolved classes, respectively. These particles were re-extracted without binning and subjected to further rounds of 2D classification, yielding 352,617/465,180/397,238 particles selected for ab initio reconstruction. Further rounds of heterogeneous refinement using decoy references were performed to enrich high-quality particles for subsequent reconstruction. Finally, non-uniform refinement of 152,254/193,634/297,954 selected particles yielded cryo-EM reconstructions of apo hVIAAT, the apo hVIAAT–LAMP5 complex, and the GABA-bound hVIAAT–LAMP5 complex at resolutions of 3.4, 3.0 and 2.9 Å, respectively.

Model building and refinement

Full-length models of UNC-47, UNC-46, hVIAAT, and LAMP5 predicted individually using

Langtaosha (LTS) Preprint doi: https://doi.org/10.65215/LTSpreprints.2026.11.02.000378. This version posted November 2, 2026. The copyright holder for this preprint (which was not certified by peer review) is the author/funder. All Rights Reserved. No reuse allowed without permission.

AlphaFold 3 were used as initial templates for model building. The predicted models were first docked into the corresponding cryo-EM density maps using UCSF ChimeraX[58], followed by global relaxation in ISOLDE[59]. The models were then manually inspected, adjusted, and trimmed in COOT[60] to improve their fit to the experimental densities. Owing to the limited local resolution, the N-terminal extracellular domain of LAMP5 was docked in the EM map without side chains. Real-space refinement against the corresponding maps was performed using PHENIX. Further model optimization was carried out in ISOLDE, followed by a final round of real-space refinement in PHENIX[61]. Detailed model refinement and validation statistics are provided in Supplementary Table S4.

Phylogenetic and evolutionary analysis

① Sequence datasets and identifier tracking

Three amino acid sequence datasets were assembled for comparative analyses: VIAAT homologues from 27 metazoan taxa, LAMP5/UNC-46 homologues from 71 taxa, and eight LAMP-family proteins from *Homo sapiens* and *Caenorhabditis elegans*. Accession identifiers were standardized against UniProtKB records. Where no exact sequence match was available in UniProtKB, the corresponding UniParc record was used.

The human-*C. elegans* LAMP-family subset comprised human LAMP1, LAMP2A, LAMP3, CD68 and LAMP5, together with *C. elegans* LMP-1, LMP-2 and UNC-46. LAMP2A was used to represent human LAMP2 in the eight-sequence phylogeny. A separate ten-sequence alignment additionally included LAMP2B and LAMP2C isoforms. Protein names,

Langtaosha (LTS) Preprint doi: https://doi.org/10.65215/LTSpreprints.2026.11.02.000378. This version posted November 2, 2026. The copyright holder for this preprint (which was not certified by peer review) is the author/funder. All Rights Reserved. No reuse allowed without permission.

UniProtKB or UniParc accession numbers, taxonomic assignments and sequence lengths are provided in Supplementary Fig. S2 and Table S3.

② Multiple-sequence alignment and domain annotation

Full-length protein sequences were aligned separately for the VIAAT, eight-sequence LAMP-family, ten-sequence LAMP-family and 71-sequence LAMP5/UNC-46 datasets. Alignments were generated using MAFFT v7.487 with automatic strategy selection (`--auto`; L-INS-i for these datasets). The LAMP-family and LAMP5/UNC-46 alignments were subsequently filtered using trimAl v1.4.rev15 with the options `-gt 0.5 -keepheader`. This procedure retained columns occupied by residues in at least 50% of the sequences while preserving the original identifiers for the corresponding IQ-TREE analyses.

Alignments were inspected in Jalview v2.11.5.1. The transmembrane boundaries of human VIAAT and *C. elegans* UNC-47 were manually verified and mapped onto the alignment. For focused sequence comparisons, alignment columns corresponding to human VIAAT residues 171-186 and the substrate-binding residues Tyr221, Phe315 and Thr318 were extracted, while retaining the residue numbering of each protein.

For LAMP-family domain schematics, signal peptides, luminal domains and transmembrane helices were manually annotated for human and *C.elegans* LAMP-family protein sequences. The assigned boundaries were used to generate domain schematics in IBS 2.0, with all proteins drawn to the same amino acid scale.

Langtaosha (LTS) Preprint doi: https://doi.org/10.65215/LTSpreprints.2026.11.02.000378. This version posted November 2, 2026. The copyright holder for this preprint (which was not certified by peer review) is the author/funder. All Rights Reserved. No reuse allowed without permission.

③ Maximum-likelihood phylogenetic inference

The final 27-sequence VIAAT phylogeny was inferred by maximum likelihood in MEGA v12.0, using the Jones-Taylor-Thornton substitution model with uniform rates across sites. All input alignment positions were included using the 'Use all sites' setting. An initial tree was generated automatically using the NJ/MP option and optimized by nearest-neighbour-interchange searches without a branch-swap filter. Branch support was assessed with 1,000 standard bootstrap replicates. The rooting procedure used for the displayed tree requires confirmation.

The final eight-sequence LAMP-family, ten-sequence LAMP-family and 71-sequence LAMP5/UNC-46 phylogenies were inferred from the corresponding trimAl-filtered alignments using IQ-TREE v3.1.4. ModelFinder was used to identify the best-fitting amino acid substitution model according to the Bayesian information criterion (`-m MFP`). The selected models were WAG+G4 for the eight-sequence alignment (362 positions), WAG+F+G4 for the ten-sequence alignment (388 positions), and Q.PFAM+I+R5 for the 71-sequence alignment (273 positions). Support was estimated with 1,000 ultrafast bootstrap replicates, with nearest-neighbour-interchange optimization of bootstrap trees enabled (`-B 1000 -bnni`). The broad LAMP5/UNC-46 tree was displayed as an unrooted tree; the layout was not used to infer evolutionary direction or ancestral states.

④ Reference species phylogenies

Langtaosha (LTS) Preprint doi: https://doi.org/10.65215/LTSpreprints.2026.11.02.000378. This version posted November 2, 2026. The copyright holder for this preprint (which was not certified by peer review) is the author/funder. All Rights Reserved. No reuse allowed without permission.

Reference species phylogenies were retrieved from TimeTree 6 using the taxon lists corresponding to the VIAAT and LAMP5/UNC-46 datasets. Redundant subspecific entries were removed, yielding trees containing 24 and 58 terminal taxa, respectively. Taxa that could not be placed by TimeTree were excluded. Where substitute entries were returned, target taxon names were retained as tip labels, whereas their placements and divergence-time estimates followed the substitute entries. Substitutions and exclusions were recorded in the accompanying taxon inventory (Supplementary Tables S2 and S6). Trees were annotated in iTOL. Divergence times were obtained from TimeTree rather than estimated from the protein sequence alignments.

⑤ AlphaFold 3 prediction of VIAAT–LAMP family complexes

Models of the VIAAT-LAMP family complexes were predicted using AlphaFold 3 through the AlphaFold Server. For each species, one copy of the full-length LAMP5/UNC-46 homologue and one copy of the corresponding full-length VIAAT homologue from the same species were submitted as a separate prediction task. Template use was enabled. Five output models were retained for each protein pair and included in the subsequent interface calculations, and the resulting interface areas were averaged for each species.

The same procedure was used to compare the predicted association of VIAAT complexed with different LAMP-family members in humans and *C.elegans*. Human VIAAT was paired individually with human LAMP1, LAMP2A, LAMP3, CD68 and LAMP5, and *C.elegans* UNC-47 with UNC-46, LMP-1 and LMP-2. The archived `model_0` output from each task

Langtaosha (LTS) Preprint doi: https://doi.org/10.65215/LTSpreprints.2026.11.02.000378. This version posted November 2, 2026. The copyright holder for this preprint (which was not certified by peer review) is the author/funder. All Rights Reserved. No reuse allowed without permission.

was used for structural visualization in UCSF ChimeraX.

⑥ Trimming of predicted terminal extensions

Terminal extension loops were removed from both chains before calculation of the interface area. Secondary structure was assigned using PyMOL v3.1.6.1 (`dss`). Qualifying helices contained ≥7 consecutive helical residues, with mean contact counts ≥1 and mean prediction-confidence scores ≥65; qualifying strands contained ≥3 consecutive strand residues, with corresponding thresholds of ≥1.5 and ≥50. Each chain was retained between its first and last qualifying segments, with up to two flanking residues at either end and all intervening loops preserved.

⑦ Calculation of luminal-core interface area

Interface calculations included the retained luminal core of each LAMP-family proteins and the entire trimmed VIAAT chain. Luminal-core boundaries were defined from database domain predictions.

The buried interface area was calculated as

$$I = [SASA(A_{core}) + SASA(B_{trimmed}) - SASA(A_{core} \cup B_{trimmed})] / 2,$$

where SASA (A_{core}) denotes the retained LAMP luminal core, $B_{trimmed}$ denotes the trimmed VIAAT chain and SASA denotes solvent-accessible surface area. SASA was calculated for each partner separately and for the combined pair using the same atomic coordinates. Division by two gives the mean surface area buried on the two partners. Calculations used the Shrake-Rupley implementation in Biopython v1.85, with its default atomic radii, a 1.4-Å

Langtaosha (LTS) Preprint doi: https://doi.org/10.65215/LTSpreprints.2026.11.02.000378. This version posted November 2, 2026. The copyright holder for this preprint (which was not certified by peer review) is the author/funder. All Rights Reserved. No reuse allowed without permission.

solvent probe and 960 sampling points per atom. Only heavy atoms were included, and no additional residue-distance cutoff was applied.

The arithmetic mean was used as the species-level value, and the sample standard deviation described variation among the five predictions. Retained-core residue counts and coverage fractions were recorded for each model to document any loss of annotated core residues during trimming (Table 5). Interface areas were interpreted as geometric measures of the predicted complexes; zero values indicate no sampled surface burial under these calculation settings.

⑧ Phylogeny-based visualization of structural features

Protein and reference species trees were annotated in iTOL. Continuous interface areas and categorical connector states were mapped onto the 71-tip LAMP5/UNC-46 protein tree using TreeAndLeaf v1.24.0 and RedeR v3.8.1 in R v4.6.1, with ape v5.8-1 and igraph v2.3.4. Protein identifiers were used to match model-derived measurements to tree tips. Interface areas were mapped to a continuous nine-colour purple palette spanning 0-1,172.9 Å^2.

For the classification of the luminal–transmembrane connecting region, the linker connecting the LAMP luminal domain to its transmembrane helix was classified by visual inspection of a representative structure for each species. Assignments were recorded as straight, straight (loop), bent or bent (loop). The species-level assignments were mapped onto the phylogeny using categorical node colours and uniform node sizes.

Langtaosha (LTS) Preprint doi: https://doi.org/10.65215/LTSpreprints.2026.11.02.000378. This version posted November 2, 2026. The copyright holder for this preprint (which was not certified by peer review) is the author/funder. All Rights Reserved. No reuse allowed without permission.

Reciprocal pull-down assays and immunoblotting

Reciprocal pull-down assays were performed to evaluate interactions between VIAAT proteins and their LAMP-family partners. N-terminally FLAG-tagged hVIAAT and N-terminally Strep-tagged LAMP5 were co-expressed in HEK293F suspension cells and extracted as described above. Three combinations were examined: wild-type hVIAAT with wild-type LAMP5, wild-type hVIAAT with LAMP5(R230A/Y256A), and hVIAAT(S239A) with LAMP5(R230A/Y256A).

Following centrifugation at 16,000 rpm for 1 h at 4 °C, the clarified supernatant was divided into two aliquots and incubated separately with anti-FLAG M2 affinity gel (Sigma-Aldrich) or Strep-Tactin Sepharose (IBA) to capture hVIAAT or LAMP5, respectively. The resins were washed five times with wash buffer containing 25 mM Tris-HCl pH 7.5, 150 mM NaCl, 1.3 mg mL^{-1} aprotinin, 0.7 mg mL^{-1} pepstatin A, 5 mg mL^{-1} leupeptin and 0.01% (w/v) LMNG. Bound proteins were eluted with wash buffer supplemented with either 0.4 mg mL^{-1} FLAG peptide for the anti-FLAG M2 affinity gel or 2 mg mL^{-1} desthiobiotin (IBA) for Strep-Tactin Sepharose.

Eluted proteins were separated by SDS-PAGE and transferred onto polyvinylidene difluoride (PVDF) membranes (Millipore). Membranes were blocked with 5% (w/v) skimmed milk in Tris-buffered saline containing Tween-20 (TBST) and incubated with mouse anti-FLAG (MBL Biotech) or rabbit anti-Strep (HUABIO) primary antibodies to detect hVIAAT or

Langtaosha (LTS) Preprint doi: https://doi.org/10.65215/LTSpreprints.2026.11.02.000378. This version posted November 2, 2026. The copyright holder for this preprint (which was not certified by peer review) is the author/funder. All Rights Reserved. No reuse allowed without permission.

LAMP5, respectively. After three washes with TBST, the membranes were incubated with the corresponding HRP-conjugated goat anti-mouse (BBI) or goat anti-rabbit (HUABIO) IgG secondary antibodies. Immunoreactive bands were detected using SuperKine ultrasensitive ECL luminescence reagent (Abbkine) and visualized using an Amersham ImageQuant 800 imaging system (Cytiva).

The same reciprocal pull-down procedure was applied to assess interactions of UNC-47 with UNC-46 and the interactions of hVIAAT or UNC-47 with two LAMP5–UNC-46 domain-swapped chimeras. The chimeric constructs were generated by PCR-based assembly and verified by Sanger sequencing. The LAMP5 LD–UNC-46 TM chimera comprised the luminal domain of LAMP5 (residues 1–210) fused to the transmembrane and membrane-proximal region of UNC-46 (residues 192–260), including helices H1′ and H2′. Conversely, the UNC-46 LD–LAMP5 TM chimera comprised the luminal domain of UNC-46 (residues 1–191) fused to the transmembrane region of LAMP5 (residues 211–280). Each chimera was co-expressed separately with hVIAAT or UNC-47. Both transporters carried an N-terminal FLAG tag. The LAMP5 LD–UNC-46 TM chimera carried an N-terminal Strep tag, whereas wild-type UNC-46 and the UNC-46 LD–LAMP5 TM chimera were instead tagged at their C-terminus to avoid loss of the affinity tag upon cleavage of the N-terminal signal peptide.

Thermal stability analysis

The thermal stability of the purified hVIAAT–LAMP5 complex and the indicated hVIAAT substrate-binding variants (Y221A, Y221F, F315A, and T318A) was assessed using the

Langtaosha (LTS) Preprint doi: https://doi.org/10.65215/LTSpreprints.2026.11.02.000378. This version posted November 2, 2026. The copyright holder for this preprint (which was not certified by peer review) is the author/funder. All Rights Reserved. No reuse allowed without permission.

UNcle Protein Stability Screening Platform (Unchained Labs). Purified proteins were diluted to 0.5 mg mL^{-1} in buffer containing 50 mM Tris-HCl pH 7.5, 150 mM NaCl, and 0.005% (w/v) LMNG. Samples were prepared in the presence or absence of 500 mM GABA and incubated on ice for 30 min before measurement.

Intrinsic protein fluorescence was monitored during heating from 25 to 95 °C at a rate of 0.8 °C min^{-1}. The apparent melting temperature (T_m) was determined from the principal peak of the first derivative of the barycentric mean fluorescence wavelength with respect to temperature (dBCM/dT). GABA-induced thermal shifts were calculated as $\Delta T_m = T_{m,\ with\ GABA} - T_{m,\ without\ GABA}$. Data are presented as mean ± s.e.m., and statistical significance was assessed using two-tailed unpaired t-tests in GraphPad Prism 10.4.1.

Prediction of the pKa and protonation state of Glu213

Structures of human VIAAT in three conformational states were first prepared using the Protein Preparation Wizard in Schrödinger Suite 2025-1[62]. Hydrogen atoms were added, and the hydrogen-bond network was optimized at a reference pH of 7.0. For the luminal-occluded structure, GABA was retained in the substrate-binding pocket and processed with Epik at pH 7.0 ± 1.0[63]. The pKa of Glu213 was then estimated independently for each prepared structure using PROPKA 3.5.1[64], with the added hydrogen atoms retained. The predicted fraction of protonated Glu213 (GLH form) at a given pH was calculated using a derived Henderson-Hasselbalch equation:

$$f_{GLH} = \frac{[GLH]}{[GLH]+[GLU^-]} = \frac{1}{1+10^{(pH-pKa)}} \quad (1)$$

Langtaosha (LTS) Preprint doi: https://doi.org/10.65215/LTSpreprints.2026.11.02.000378. This version posted November 2, 2026. The copyright holder for this preprint (which was not certified by peer review) is the author/funder. All Rights Reserved. No reuse allowed without permission.

Thus, the predicted fraction of deprotonated Glu213 (GLU^- form) was $1 - f_{GLH}$. Both fractions were calculated at pH 5.5 and 7.2, representing the specified conditions for the synaptic-vesicle lumen and presynaptic cytosol, respectively.

Data availability

The cryo-EM maps reported in this study have been deposited in the Electron Microscopy Data Bank (EMDB) under the following accession codes: EMD-84563 (hVIAAT in apo state), EMD-84561 (the hVIAAT-LAMP5 complex in apo state), EMD-84560 (GABA-bound hVIAAT-LAMP5 complex), EMD-84567 (UNC-47 in apo state), and EMD-84566 (the UNC-47-UNC-46 complex in apo state). The corresponding atomic coordinates have been deposited in the Protein Data Bank (PDB) under accession codes 47NZ, 47NX, 47NW, 47OD, and 47OC, respectively. Additional data supporting the findings of this study are available from the corresponding author upon reasonable request.

Langtaosha (LTS) Preprint doi: https://doi.org/10.65215/LTSpreprints.2026.11.02.000378. This version posted November 2, 2026. The copyright holder for this preprint (which was not certified by peer review) is the author/funder. All Rights Reserved. No reuse allowed without permission.

Reference

1 Shu, Y., Hasenstaub, A. & McCormick, D. A. Turning on and off recurrent balanced cortical activity. *Nature* **423**, 288-293 (2003). https://doi.org/10.1038/nature01616

2 Haider, B., Duque, A., Hasenstaub, A. R. & McCormick, D. A. Neocortical network activity in vivo is generated through a dynamic balance of excitation and inhibition. *J Neurosci* **26**, 4535-4545 (2006). https://doi.org/10.1523/jneurosci.5297-05.2006

3 Yizhar, O. *et al.* Neocortical excitation/inhibition balance in information processing and social dysfunction. *Nature* **477**, 171-178 (2011). https://doi.org/10.1038/nature10360

4 Han, S. *et al.* Autistic-like behaviour in Scn1a+/- mice and rescue by enhanced GABA-mediated neurotransmission. *Nature* **489**, 385-390 (2012). https://doi.org/10.1038/nature11356

5 Selimbeyoglu, A. *et al.* Modulation of prefrontal cortex excitation/inhibition balance rescues social behavior in CNTNAP2-deficient mice. *Sci Transl Med* **9** (2017). https://doi.org/10.1126/scitranslmed.aah6733

6 Cho, K. K. *et al.* Gamma rhythms link prefrontal interneuron dysfunction with cognitive inflexibility in Dlx5/6(+/-) mice. *Neuron* **85**, 1332-1343 (2015). https://doi.org/10.1016/j.neuron.2015.02.019

7 Sawada, T. *et al.* Developmental excitation-inhibition imbalance underlying psychoses revealed by single-cell analyses of discordant twins-derived cerebral organoids. *Mol Psychiatry* **25**, 2695-2711 (2020). https://doi.org/10.1038/s41380-020-0844-z

8 Wojcik, S. M. *et al.* A shared vesicular carrier allows synaptic corelease of GABA and glycine. *Neuron* **50**, 575-587 (2006). https://doi.org/10.1016/j.neuron.2006.04.016

9 McIntire, S. L., Reimer, R. J., Schuske, K., Edwards, R. H. & Jorgensen, E. M. Identification and characterization of the vesicular GABA transporter. *Nature* **389**, 870-876 (1997). https://doi.org/10.1038/39908

10 Sagne, C. *et al.* Cloning of a functional vesicular GABA and glycine transporter by screening of genome databases. *FEBS Lett* **417**, 177-183 (1997). https://doi.org/10.1016/s0014-5793(97)01279-9

11 Chaudhry, F. A. *et al.* The vesicular GABA transporter, VGAT, localizes to synaptic vesicles in sets of glycinergic as well as GABAergic neurons. *J Neurosci* **18**, 9733-9750 (1998). https://doi.org/10.1523/jneurosci.18-23-09733.1998

12 Dumoulin, A. *et al.* Presence of the vesicular inhibitory amino acid transporter in GABAergic and glycinergic synaptic terminal boutons. *J Cell Sci* **112 (Pt 6)**, 811-823 (1999). https://doi.org/10.1242/jcs.112.6.811

13 Jonas, P., Bischofberger, J. & Sandkuhler, J. Corelease of two fast neurotransmitters at a central synapse. *Science* **281**, 419-424 (1998). https://doi.org/10.1126/science.281.5375.419

14 Heron, S. E. *et al.* Association of SLC32A1 Missense Variants With Genetic Epilepsy With Febrile Seizures Plus. *Neurology* **96**, e2251-e2260 (2021). https://doi.org/10.1212/wnl.0000000000011855

15 Platzer, K. *et al.* De Novo Missense Variants in SLC32A1 Cause a Developmental and Epileptic Encephalopathy Due to Impaired GABAergic Neurotransmission. *Ann Neurol* **92**, 958-973 (2022). https://doi.org/10.1002/ana.26485

16 Gasnier, B. The SLC32 transporter, a key protein for the synaptic release of inhibitory amino acids. *Pflugers Arch* **447**, 756-759 (2004). https://doi.org/10.1007/s00424-003-1091-2

17 Pidathala, S. *et al.* Mechanisms of neurotransmitter transport and drug inhibition in human

Langtaosha (LTS) Preprint doi: https://doi.org/10.65215/LTSpreprints.2026.11.02.000378. This version posted November 2, 2026. The copyright holder for this preprint (which was not certified by peer review) is the author/funder. All Rights Reserved. No reuse allowed without permission.

VMAT2. *Nature* **623**, 1086-1092 (2023). https://doi.org/10.1038/s41586-023-06727-9

18 Wu, D. *et al.* Transport and inhibition mechanisms of human VMAT2. *Nature* **626**, 427-434 (2024). https://doi.org/10.1038/s41586-023-06926-4

19 Wang, Y. *et al.* Transport and inhibition mechanism for VMAT2-mediated synaptic vesicle loading of monoamines. *Cell Res* **34**, 47-57 (2024). https://doi.org/10.1038/s41422-023-00906-z

20 Ye, J. *et al.* Structural insights into vesicular monoamine storage and drug interactions. *Nature* **629**, 235-243 (2024). https://doi.org/10.1038/s41586-024-07290-7

21 Im, D. *et al.* Neurotransmitter recognition by human vesicular monoamine transporter 2. *Nat Commun* **15**, 7661 (2024). https://doi.org/10.1038/s41467-024-51960-z

22 Zhang, Y. *et al.* Structural insights into VAChT neurotransmitter recognition and inhibition. *Cell Res* **34**, 665-668 (2024). https://doi.org/10.1038/s41422-024-00986-5

23 Ma, Q. *et al.* Binding mechanism and antagonism of the vesicular acetylcholine transporter VAChT. *Nat Struct Mol Biol* **32**, 818-827 (2025). https://doi.org/10.1038/s41594-024-01462-9

24 Li, F. *et al.* Ion transport and regulation in a synaptic vesicle glutamate transporter. *Science* **368**, 893-897 (2020). https://doi.org/10.1126/science.aba9202

25 Li, F. *et al.* Substrate recognition and allosteric regulation of synaptic vesicle glutamate transporter VGLUT2. *Nat Struct Mol Biol* **32**, 1479-1487 (2025). https://doi.org/10.1038/s41594-025-01568-8

26 Zhang, Y. & Zhang, Z. Structural basis of VAChT inhibition by spiroindolines and alkylsulfones. *Structure* **34**, 123-132.e124 (2026). https://doi.org/10.1016/j.str.2025.10.005

27 Martens, H. *et al.* Unique luminal localization of VGAT-C terminus allows for selective labeling of active cortical GABAergic synapses. *J Neurosci* **28**, 13125-13131 (2008). https://doi.org/10.1523/jneurosci.3887-08.2008

28 Blakely, R. D. & Edwards, R. H. Vesicular and plasma membrane transporters for neurotransmitters. *Cold Spring Harb Perspect Biol* **4** (2012). https://doi.org/10.1101/cshperspect.a005595

29 Cidon, S. & Sihra, T. S. Characterization of a H+-ATPase in rat brain synaptic vesicles. Coupling to L-glutamate transport. *J Biol Chem* **264**, 8281-8288 (1989).

30 Knoth, J., Zallakian, M. & Njus, D. Stoichiometry of H+-linked dopamine transport in chromaffin granule ghosts. *Biochemistry* **20**, 6625-6629 (1981). https://doi.org/10.1021/bi00526a016

31 Nguyen, M. L., Cox, G. D. & Parsons, S. M. Kinetic parameters for the vesicular acetylcholine transporter: two protons are exchanged for one acetylcholine. *Biochemistry* **37**, 13400-13410 (1998). https://doi.org/10.1021/bi9802263

32 Maycox, P. R., Deckwerth, T., Hell, J. W. & Jahn, R. Glutamate uptake by brain synaptic vesicles. Energy dependence of transport and functional reconstitution in proteoliposomes. *J Biol Chem* **263**, 15423-15428 (1988).

33 Schenck, S., Wojcik, S. M., Brose, N. & Takamori, S. A chloride conductance in VGLUT1 underlies maximal glutamate loading into synaptic vesicles. *Nat Neurosci* **12**, 156-162 (2009). https://doi.org/10.1038/nn.2248

34 Preobraschenski, J., Zander, J. F., Suzuki, T., Ahnert-Hilger, G. & Jahn, R. Vesicular glutamate transporters use flexible anion and cation binding sites for efficient accumulation of neurotransmitter. *Neuron* **84**, 1287-1301 (2014). https://doi.org/10.1016/j.neuron.2014.11.008

35 Eriksen, J. *et al.* Protons Regulate Vesicular Glutamate Transporters through an Allosteric

Langtaosha (LTS) Preprint doi: https://doi.org/10.65215/LTSpreprints.2026.11.02.000378. This version posted November 2, 2026. The copyright holder for this preprint (which was not certified by peer review) is the author/funder. All Rights Reserved. No reuse allowed without permission.

Mechanism. *Neuron* **90**, 768-780 (2016). https://doi.org/10.1016/j.neuron.2016.03.026

36 Kolen, B. *et al.* Vesicular glutamate transporters are H(+)-anion exchangers that operate at variable stoichiometry. *Nat Commun* **14**, 2723 (2023). https://doi.org/10.1038/s41467-023-38340-9

37 Fykse, E. M. & Fonnum, F. Uptake of gamma-aminobutyric acid by a synaptic vesicle fraction isolated from rat brain. *J Neurochem* **50**, 1237-1242 (1988). https://doi.org/10.1111/j.1471-4159.1988.tb10599.x

38 Hell, J. W., Maycox, P. R., Stadler, H. & Jahn, R. Uptake of GABA by rat brain synaptic vesicles isolated by a new procedure. *Embo j* **7**, 3023-3029 (1988). https://doi.org/10.1002/j.1460-2075.1988.tb03166.x

39 Kish, P. E., Fischer-Bovenkerk, C. & Ueda, T. Active transport of gamma-aminobutyric acid and glycine into synaptic vesicles. *Proc Natl Acad Sci U S A* **86**, 3877-3881 (1989). https://doi.org/10.1073/pnas.86.10.3877

40 Hell, J. W., Maycox, P. R. & Jahn, R. Energy dependence and functional reconstitution of the gamma-aminobutyric acid carrier from synaptic vesicles. *J Biol Chem* **265**, 2111-2117 (1990).

41 Farsi, Z. *et al.* Single-vesicle imaging reveals different transport mechanisms between glutamatergic and GABAergic vesicles. *Science* **351**, 981-984 (2016). https://doi.org/10.1126/science.aad8142

42 Egashira, Y. *et al.* Unique pH dynamics in GABAergic synaptic vesicles illuminates the mechanism and kinetics of GABA loading. *Proc Natl Acad Sci U S A* **113**, 10702-10707 (2016). https://doi.org/10.1073/pnas.1604527113

43 Herman, M. A., Trimbuch, T. & Rosenmund, C. Differential pH Dynamics in Synaptic Vesicles From Intact Glutamatergic and GABAergic Synapses. *Front Synaptic Neurosci* **10**, 44 (2018). https://doi.org/10.3389/fnsyn.2018.00044

44 Juge, N., Muroyama, A., Hiasa, M., Omote, H. & Moriyama, Y. Vesicular inhibitory amino acid transporter is a Cl-/gamma-aminobutyrate Co-transporter. *J Biol Chem* **284**, 35073-35078 (2009). https://doi.org/10.1074/jbc.M109.062414

45 Nakatsu, F. *et al.* Defective function of GABA-containing synaptic vesicles in mice lacking the AP-3B clathrin adaptor. *J Cell Biol* **167**, 293-302 (2004). https://doi.org/10.1083/jcb.200405032

46 Gomes, J. R. *et al.* Cleavage of the vesicular GABA transporter under excitotoxic conditions is followed by accumulation of the truncated transporter in nonsynaptic sites. *J Neurosci* **31**, 4622-4635 (2011). https://doi.org/10.1523/jneurosci.3541-10.2011

47 Lopez-Hernandez, T. *et al.* Clathrin-independent endocytic retrieval of SV proteins mediated by the clathrin adaptor AP-2 at mammalian central synapses. *Elife* **11** (2022). https://doi.org/10.7554/eLife.71198

48 Schuske, K., Palfreyman, M. T., Watanabe, S. & Jorgensen, E. M. UNC-46 is required for trafficking of the vesicular GABA transporter. *Nat Neurosci* **10**, 846-853 (2007). https://doi.org/10.1038/nn1920

49 David, A. *et al.* BAD-LAMP defines a subset of early endocytic organelles in subpopulations of cortical projection neurons. *J Cell Sci* **120**, 353-365 (2007). https://doi.org/10.1242/jcs.03316

50 Tiveron, M. C. *et al.* LAMP5 Fine-Tunes GABAergic Synaptic Transmission in Defined Circuits of the Mouse Brain. *PLoS One* **11**, e0157052 (2016). https://doi.org/10.1371/journal.pone.0157052

51 Koebis, M. *et al.* LAMP5 in presynaptic inhibitory terminals in the hindbrain and spinal cord: a role in startle response and auditory processing. *Mol Brain* **12**, 20 (2019).

Langtaosha (LTS) Preprint doi: https://doi.org/10.65215/LTSpreprints.2026.11.02.000378. This version posted November 2, 2026. The copyright holder for this preprint (which was not certified by peer review) is the author/funder. All Rights Reserved. No reuse allowed without permission.

https://doi.org/10.1186/s13041-019-0437-4

52 Santos, M. S., Park, C. K., Foss, S. M., Li, H. & Voglmaier, S. M. Sorting of the vesicular GABA transporter to functional vesicle pools by an atypical dileucine-like motif. *J Neurosci* **33**, 10634-10646 (2013). https://doi.org/10.1523/jneurosci.0329-13.2013

53 Sankaranarayanan, S., De Angelis, D., Rothman, J. E. & Ryan, T. A. The use of pHluorins for optical measurements of presynaptic activity. *Biophys J* **79**, 2199-2208 (2000). https://doi.org/10.1016/S0006-3495(00)76468-X

54 Sankaranarayanan, S. & Ryan, T. A. Real-time measurements of vesicle-SNARE recycling in synapses of the central nervous system. *Nat Cell Biol* **2**, 197-204 (2000). https://doi.org/10.1038/35008615

55 Nachshen, D. A. & Drapeau, P. The regulation of cytosolic pH in isolated presynaptic nerve terminals from rat brain. *J Gen Physiol* **91**, 289-303 (1988). https://doi.org/10.1085/jgp.91.2.289

56 Krantz, D. E. *et al.* A phosphorylation site regulates sorting of the vesicular acetylcholine transporter to dense core vesicles. *J Cell Biol* **149**, 379-396 (2000). https://doi.org/10.1083/jcb.149.2.379

57 Waites, C. L. *et al.* An acidic motif retains vesicular monoamine transporter 2 on large dense core vesicles. *J Cell Biol* **152**, 1159-1168 (2001). https://doi.org/10.1083/jcb.152.6.1159

58 Pettersen, E. F. *et al.* UCSF ChimeraX: Structure visualization for researchers, educators, and developers. *Protein Sci* **30**, 70-82 (2021). https://doi.org/10.1002/pro.3943

59 Croll, T. I. ISOLDE: a physically realistic environment for model building into low-resolution electron-density maps. *Acta Crystallogr D Struct Biol* **74**, 519-530 (2018). https://doi.org/10.1107/S2059798318002425

60 Emsley, P., Lohkamp, B., Scott, W. G. & Cowtan, K. Features and development of Coot. *Acta Crystallogr D Biol Crystallogr* **66**, 486-501 (2010). https://doi.org/10.1107/S0907444910007493

61 Afonine, P. V. *et al.* Towards automated crystallographic structure refinement with phenix.refine. *Acta Crystallogr D Biol Crystallogr* **68**, 352-367 (2012). https://doi.org/10.1107/S0907444912001308

62 Sastry, G. M., Adzhigirey, M., Day, T., Annabhimoju, R. & Sherman, W. Protein and ligand preparation: parameters, protocols, and influence on virtual screening enrichments. *J Comput Aided Mol Des* **27**, 221-234 (2013). https://doi.org/10.1007/s10822-013-9644-8

63 Shelley, J. C. *et al.* Epik: a software program for pK(a) prediction and protonation state generation for drug-like molecules. *J Comput Aided Mol Des* **21**, 681-691 (2007). https://doi.org/10.1007/s10822-007-9133-z

64 Olsson, M. H., Sondergaard, C. R., Rostkowski, M. & Jensen, J. H. PROPKA3: Consistent Treatment of Internal and Surface Residues in Empirical pKa Predictions. *J Chem Theory Comput* **7**, 525-537 (2011). https://doi.org/10.1021/ct100578z

Langtaosha (LTS) Preprint doi: https://doi.org/10.65215/LTSpreprints.2026.11.02.000378. This version posted November 2, 2026. The copyright holder for this preprint (which was not certified by peer review) is the author/funder. All Rights Reserved. No reuse allowed without permission.

Acknowledgements

We thank the Structural Biology and Biomedical Electrophysiology Core Facilities at the Bio-Tech Center, as well as the Computing Labware for Electron-microscopy Visualization and Experimental Research (CLEVER) at the Biomedical Data Center, of Shenzhen Medical Academy of Research and Translation (SMART) for their technical support and experimental assistance. This work was funded by the National Natural Science Foundation of China (32501082 to J.H.) and the Guangdong Pearl River Talent Program (ZJQNRC20241219163128017 to J.H.). J.H. and X.F. are also supported by the start-up funding from Shenzhen Medical Academy of Research and Translation (SMART).

Author Contributions

J.H. and E.M.J. conceived the project. P.H., X.H., K.G., F.Y., X.S., F.L., Y.X., B.X., W.D., X.F., E.M.J, and J.H. designed experiments; P.H., X.H., and Y.X. carried out experiments related to cryo-EM studies, including protein expression, purification, and data acquisition; J.H. and X.F. processed the cryo-EM data, and X.F. built the atomic models; K.G. and F.L. performed the phylogenetic analysis; P.H. and F.Y. conducted the pull-down assays; X.S. performed protein thermal stability analysis. P.H., X.H., K.G., F.Y., X.S., F.L., X.F., B.X., W.D., X.F., E.M.J., and J.H. analyzed data; P.H., X.H., K.G., Y.X., B.X., X.F., and J.H. wrote the manuscript with input from all authors. All authors reviewed and approved the final manuscript.

Competing Interest

Langtaosha (LTS) Preprint doi: https://doi.org/10.65215/LTSpreprints.2026.11.02.000378. This version posted November 2, 2026. The copyright holder for this preprint (which was not certified by peer review) is the author/funder. All Rights Reserved. No reuse allowed without permission.

The authors declare no competing interests.

Langtaosha (LTS) Preprint doi: https://doi.org/10.65215/LTSpreprints.2026.11.02.000378. This version posted November 2, 2026. The copyright holder for this preprint (which was not certified by peer review) is the author/funder. All Rights Reserved. No reuse allowed without permission.

Figures and Figure Legends

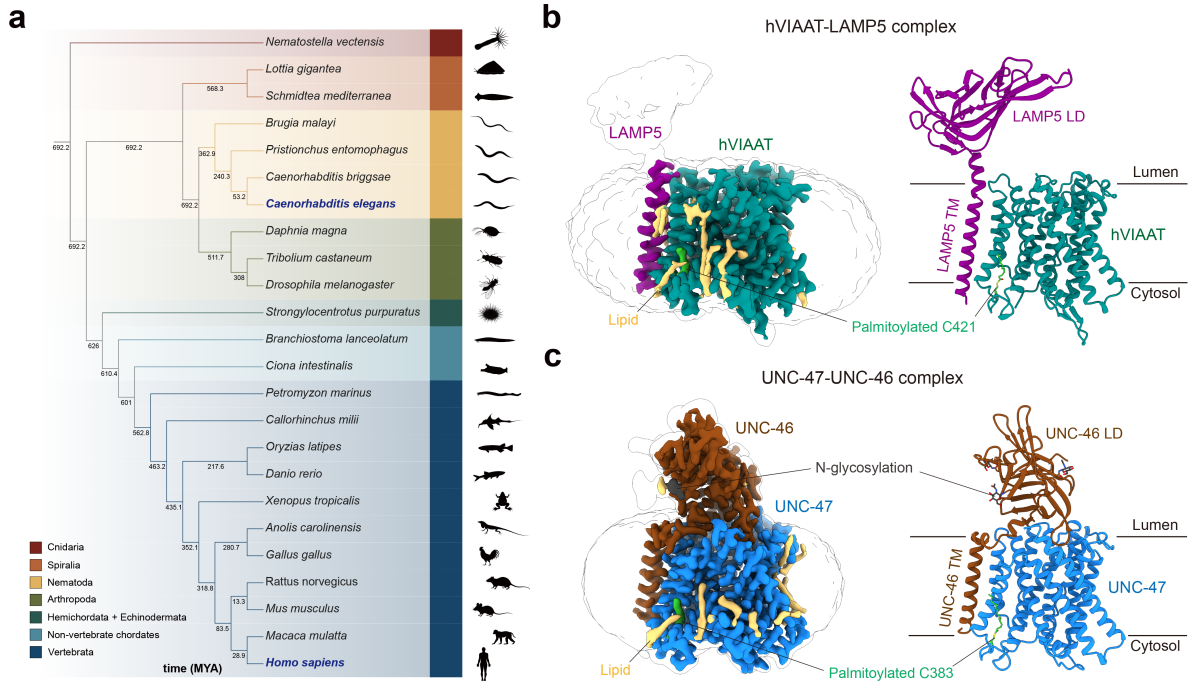


Fig. 1 | Cryo-EM structures of human and *Caenorhabditis elegans* VIAAT complexes.

a, Time-calibrated phylogenetic tree of 24 representative metazoan species constructed using divergence-time estimates from TimeTree. Branches are colored according to major taxonomic groups, with species selected for structural analysis highlighted in blue. Numerical annotations indicate estimated divergence times in millions of years ago (MYA). **b,** Cryo-EM density map (*left*) and corresponding atomic model (*right*) of the apo human VIAAT-LAMP5 complex. hVIAAT and LAMP5 are colored teal and magenta, respectively, with associated lipid densities shown in yellow. Palmitoylated Cys421 of hVIAAT is highlighted in light green. Approximate membrane boundaries are indicated. The cryo-EM map is displayed at a contour level of 4σ. **c,** Cryo-EM density map (*left*) and corresponding atomic model (*right*) of the apo *C. elegans* UNC-47–UNC-46 complex. UNC-47 and UNC-46 are colored blue and brown, respectively, with associated lipid densities shown in yellow. Palmitoylated Cys383 of UNC-47 and the resolved N-linked glycans of UNC-46 are highlighted in light green and

Langtaosha (LTS) Preprint doi: https://doi.org/10.65215/LTSpreprints.2026.11.02.000378. This version posted November 2, 2026. The copyright holder for this preprint (which was not certified by peer review) is the author/funder. All Rights Reserved. No reuse allowed without permission.

dark gray, respectively. The cryo-EM map is displayed at a contour level of 4 σ. All structural representations were prepared using UCSF ChimeraX[58] and PyMOL (Schrödinger, LLC).

Langtaosha (LTS) Preprint doi: https://doi.org/10.65215/LTSpreprints.2026.11.02.000378. This version posted November 2, 2026. The copyright holder for this preprint (which was not certified by peer review) is the author/funder. All Rights Reserved. No reuse allowed without permission.

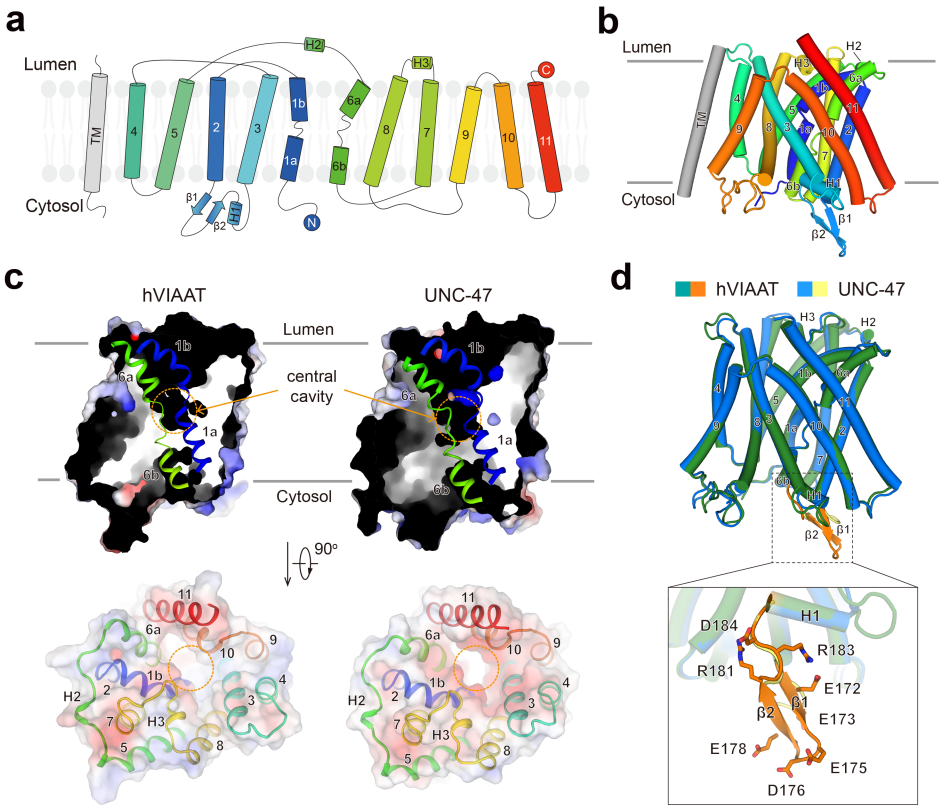


Fig. 2 | Architecture of the human and *C. elegans* VIAAT transport cores. **a,** Membrane topology of human VIAAT, illustrating its 11 transmembrane helices (TMs), the discontinuous regions of TM1 and TM6, and the cytosolic and luminal structural elements. The transmembrane helices are colored in a rainbow spectrum from the amino to the carboxy terminus. **b**, Side view of the hVIAAT transport core, with transmembrane helices represented as cylinders and colored as in **a**. **c**, Luminal-open conformations of the apo hVIAAT and UNC-47 transport cores. *Top*: Cross-sectional views of the electrostatic surfaces of hVIAAT (*left*) and UNC-47 (*right*), with positively and negatively charged regions colored blue and red, respectively. The central cavities are highlighted by orange dashed circles, and the cavity lining TM1 and TM6 helices are shown as cartoons and colored as in **a** and **b**. *Bottom*: Views of hVIAAT (*left*) and UNC-47 (*right*) from the luminal side. **d**, Structural superposition of the conserved transport cores of hVIAAT and UNC-47, revealing a

Langtaosha (LTS) Preprint doi: https://doi.org/10.65215/LTSpreprints.2026.11.02.000378. This version posted November 2, 2026. The copyright holder for this preprint (which was not certified by peer review) is the author/funder. All Rights Reserved. No reuse allowed without permission.

prominent difference in the cytosolic loop, which is extended in hVIAAT but considerably shorter in UNC-47. *Inset*: Close-up view of the cytosolic loop connecting TM2 and the H1 helix in hVIAAT. This region comprises two antiparallel β-strands (β1 and β2) and is enriched in charged residues, including Glu172, Glu173, Glu175, Asp176, Glu178, Arg181, Arg183 and Asp184.

Langtaosha (LTS) Preprint doi: https://doi.org/10.65215/LTSpreprints.2026.11.02.000378. This version posted November 2, 2026. The copyright holder for this preprint (which was not certified by peer review) is the author/funder. All Rights Reserved. No reuse allowed without permission.

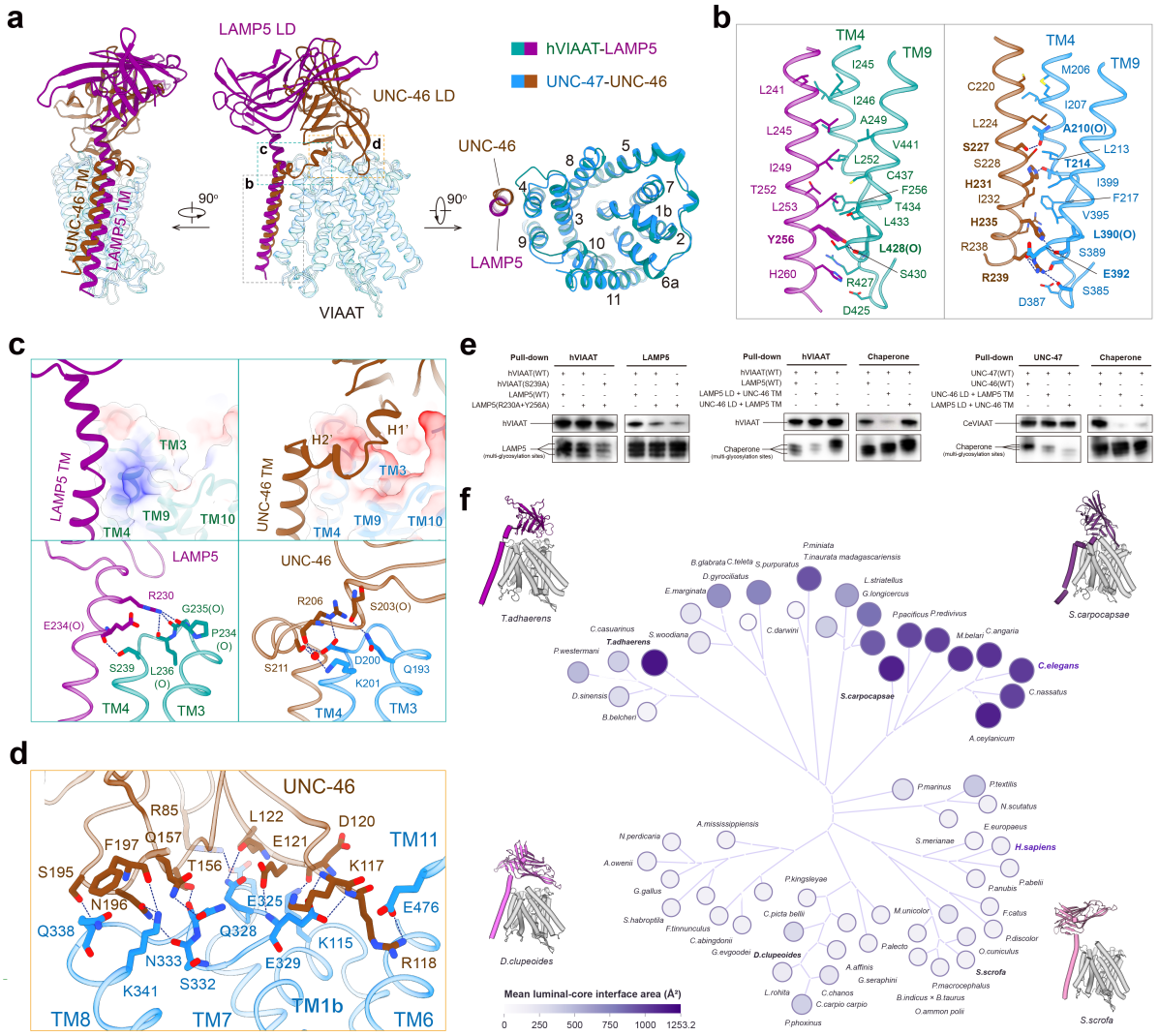


Fig. 3 | Distinct modes of VIAAT assembly with LAMP5 and UNC-46. **a,** Structural comparison of the hVIAAT–LAMP5 and UNC-47–UNC-46 complexes. The VIAAT transport cores were superimposed to illustrate the distinct orientations of LAMP5 (magenta) and UNC-46 (brown). Boxed regions are shown in detail in **b-d**. **b**, Close-up views of the transmembrane interfaces between hVIAAT and LAMP5 (*left*) and between UNC-47 and UNC-46 (*right*). Interacting residues are shown as sticks, with hydrogen bonds and polar interactions indicated by blue dashed lines. **c**, Structural comparison of the membrane-proximal interfaces. *Top*: The transmembrane helix of LAMP5 interacts with TM4 and the TM3-TM4 loop (L3-4) of hVIAAT, whereas UNC-46 adopts a bent membrane-proximal

Langtaosha (LTS) Preprint doi: https://doi.org/10.65215/LTSpreprints.2026.11.02.000378. This version posted November 2, 2026. The copyright holder for this preprint (which was not certified by peer review) is the author/funder. All Rights Reserved. No reuse allowed without permission.

conformation, with helices H1' and H2' engaging the corresponding surface of UNC-47. *Bottom*: Detailed interactions at each interface. **d**, Extensive contacts between the luminal domain (LD) of UNC-46 and UNC-47. Interacting residues are shown as sticks, with polar interactions indicated by blue dashed lines. **e**, Pull-down assays assessing complex formation between VIAAT proteins and their respective LAMP-family partners under the indicated conditions. Mutations and domain-swapped variants designed to disrupt the binding interfaces impair complex formation. Multiple bands corresponding to LAMP5 or UNC-46 reflect distinct glycosylated forms. Please refer to the Materials and Methods section for experimental details. **f**, Phylogenetic comparison of LAMP-family proteins from representative species, integrating structural predictions of their interactions with VIAAT transport cores. Node color and size indicate the mean buried interface area between the luminal domains of LAMP-family proteins and their corresponding VIAAT transport core, calculated from AlphaFold 3-predicted complex models and represented according to the scale below the tree. Representative predicted complexes spanning a range of buried interface areas are shown alongside the phylogenetic tree.

Langtaosha (LTS) Preprint doi: https://doi.org/10.65215/LTSpreprints.2026.11.02.000378. This version posted November 2, 2026. The copyright holder for this preprint (which was not certified by peer review) is the author/funder. All Rights Reserved. No reuse allowed without permission.

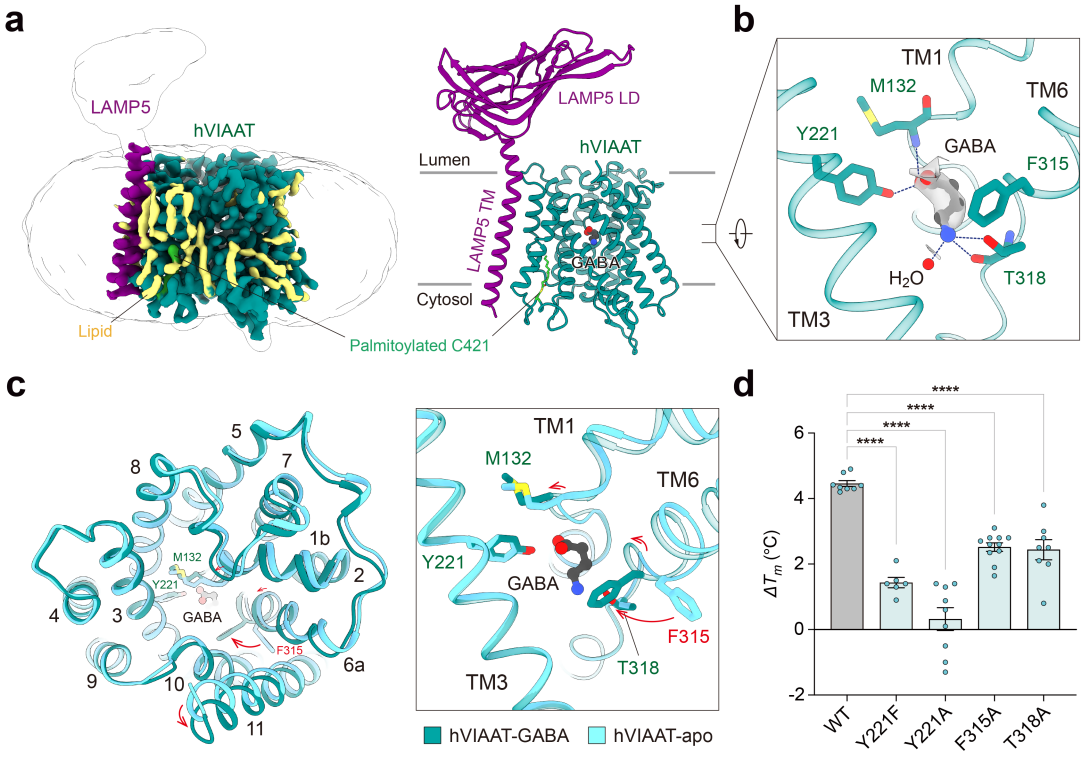


Fig. 4 | Structural basis of GABA recognition by human VIAAT. **a,** Cryo-EM density map (*left*) and corresponding atomic model (*right*) of the GABA-bound hVIAAT–LAMP5 complex. hVIAAT and LAMP5 are colored teal and magenta, respectively, with associated lipid densities shown in yellow. GABA is represented as spheres within the central substrate-binding pocket, and the conserved palmitoylated Cys421 of hVIAAT is highlighted in light green. The cryo-EM map is displayed at a contour level of 4σ. **b**, Coordination of GABA in the central binding pocket. GABA is shown in a stick-and-sphere representation, with coordinating residues depicted as sticks. The cryo-EM density corresponding to GABA is shown as a semi-transparent gray surface contour at 3.5σ. A resolved water molecule involved in GABA recognition is shown as a red sphere. **c**, Structural comparison of the GABA-bound (teal) and apo (cyan) hVIAAT structures. The overall superposition is shown from the luminal side (*left*), with the close-up view of the substrate-binding pocket (*right*) highlights local conformational rearrangements upon GABA binding. The major side-chain

Langtaosha (LTS) Preprint doi: https://doi.org/10.65215/LTSpreprints.2026.11.02.000378. This version posted November 2, 2026. The copyright holder for this preprint (which was not certified by peer review) is the author/funder. All Rights Reserved. No reuse allowed without permission.

and backbone movements are indicated by red arrows. **d**, GABA-induced thermal stabilization of purified wild-type (WT) hVIAAT and the indicated binding-site variants. The changes in melting temperature (ΔT_m) were 4.46 ± 0.09 °C for WT, 1.43 ± 0.16 °C for Y221F, 0.32 ± 0.35 °C for Y221A, 2.52 ± 0.13 °C for F315A and 2.44 ± 0.31 °C for T318A (*n* = 8, 6, 9, 11 and 8 independent measurements, respectively). Data are presented as mean ± s.e.m., with individual data points representing independent measurements. Statistical significance was assessed by one-way ANOVA; ****P < 0.0001.

Langtaosha (LTS) Preprint doi: https://doi.org/10.65215/LTSpreprints.2026.11.02.000378. This version posted November 2, 2026. The copyright holder for this preprint (which was not certified by peer review) is the author/funder. All Rights Reserved. No reuse allowed without permission.

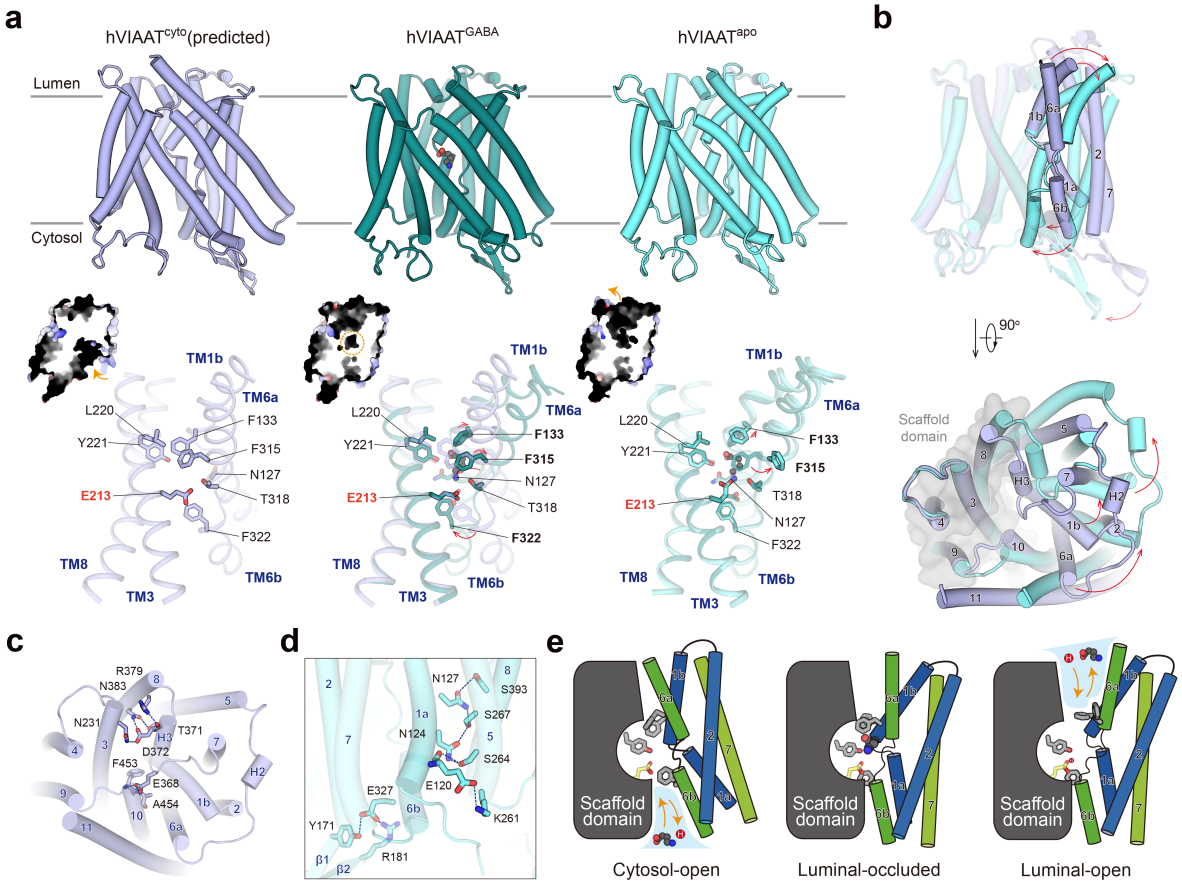


Fig. 5 | Conformational transitions underlying VIAAT-mediated substrate transport.

a, Comparison of the AlphaFold 3-predicted putative cytosol-open model with the experimentally determined GABA-bound and apo hVIAAT structures. *Top*: Side views of the overall structures, with transmembrane helices represented as cylinders. *Bottom*: Cross-sectional views of the electrostatic surfaces and central substrate-binding regions lined by TM1, TM3, TM6 and TM8. Selected gating residues are shown as sticks. Glu213, a putative proton-coupling residue, is highlighted in red. Conformational changes in gating residues associated with transitions between states are indicated by red arrows. **b**, Superposition of the putative cytosol-open model and the apo luminal-open structure following alignment of their scaffold domains, viewed from the side parallel to the membrane (*top*) and the luminal side (*bottom*). The scaffold domain is represented as semi-transparent cartoons and a grey surface.

Langtaosha (LTS) Preprint doi: https://doi.org/10.65215/LTSpreprints.2026.11.02.000378. This version posted November 2, 2026. The copyright holder for this preprint (which was not certified by peer review) is the author/funder. All Rights Reserved. No reuse allowed without permission.

Red arrows indicate movements of the transport bundle relative to the scaffold domain. **c**, Interactions within the luminal vestibule of the putative cytosol-open model. Residues forming contacts predicted to stabilize the cytosol-open conformation are shown as sticks, with polar interactions indicated by blue dashed lines. **d**, Close-up view of the cytosolic polar interaction network in the luminal-open structure. Interacting residues are shown as sticks, with polar interactions indicated by blue dashed lines. **e**, Proposed alternating-access model for VIAAT-mediated substrate transport. Key structural elements and gating residues associated with transitions among the cytosol-open, luminal-occluded, and luminal-open states are highlighted. TM1 and TM6, together with the associated TM2 and TM7 helices, are represented as cylinders. The scaffold domain is shown in grey, and the substrate GABA and coupled proton are depicted as spheres.